Progress in Oceanography xxx (2014) xxx–xxx

Contents lists available at ScienceDirect

Progress in Oceanography

journal homepage: www.elsevier.com/locate/pocean

The March 11, 2011 Tōhoku M9.0 earthquake-induced tsunami and coastal inundation along the Japanese coast: A model assessment

Changsheng Chen [a,c,g,*], Zhigang Lai [b], Robert C. Beardsley [c], Jun Sasaki [d], Jian Lin [e], Huichan Lin [a,g], Rubao Ji [f,g], Yunfang Sun [a]

[a] School for Marine Science and Technology, University of Massachusetts-Dartmouth, New Bedford, MA 02748, USA
[b] School of Marine Sciences, Sun Yat-Sen University, Guangzhou 510275, China
[c] Department of Physical Oceanography, Woods Hole Oceanographic Institution, Woods Hole, MA 02543, USA
[d] Department of Socio-Cultural Environmental Studies, Graduate School of Frontier Sciences, The University of Tokyo, Kashiwanoha, Kashiwa, Chiba 277-8563, Japan
[e] Department of Geology & Geophysics, Woods Hole Oceanographic Institution, Woods Hole, MA 02543, USA
[f] Biology Department, Woods Hole Oceanographic Institution, Woods Hole, MA 02543, USA
[g] International Center for Marine Studies, Shanghai Ocean University, Shanghai 201306, China

ARTICLE INFO

Article history:
Received 10 December 2013
Received in revised form 17 January 2014
Accepted 17 January 2014
Available online xxxx

ABSTRACT

A high-resolution nested global-Japan coastal FVCOM system was used to simulate the March 11, 2011 Tōhoku M9 earthquake-induced tsunami waves and coastal inundation along the northeastern coast of Honshu Island in the western Pacific Ocean. Experiments were made with initial fields provided by five seismic rupture models under realistic conditions with inclusion of the Kuroshio, tides and wind forcing. Results show that the model-computed intensities and distributions of tsunami waves and subsequent coastal inundation could be significantly influenced by initial conditions, even though all five cases were capable of reproducing key features of the tsunami waves. Modeled tsunami waves featured a low dispersive, weakly nonlinear long wave controlled by hydrostatic dynamics. Non-hydrostatic effects only became significant when tsunami waves reached the inner shelf and the amplitude of the leading tsunami wave grew within O(1) of the local water depth (10 m or shallower). In both hydrostatic and non-hydrostatic cases, significant mixing occurred when the ratio of wave amplitude to local water depth grew to about 0.25 or greater. Model-predicted run-up was in good agreement with 2-D *N*-wave analytical solutions on the northern coast around South Iwate where inundation was small, but not in the central Sendai coastal region where inundation was large and 3-D wave dynamics became significant. The experiments suggest that once local bathymetry is accurately configured and the intensity and shape of the initial bottom movement can be predicted, this nested FVCOM system is capable of making accurate predictions of tsunami waves and coastal inundation.

1. Introduction

March 11, 2011 was a tragic day for Japan and the world. The M9.0 and M7.9 earthquakes occurred roughly 70 km east of the Pacific coast of Tōhoku, Japan (Hayes, 2011; Simons et al., 2011) (Fig. 1), which produced a major tsunami, rapid coastal inundation, and caused serious damage in the coastal zone resulting in 15,883 people deaths, ~6146 injured and ~2,654 missing (http://www.npa.go.jp/archive/keibi/biki/higaijokyo.pdf). The tsunami also caused major infrastructure damage at the Fukushima Dai-ichi Nuclear Power Plant (FDNPP) with the meltdown of three reactors and major release of radiation into the air and coastal waters around the plant. The radionuclide leaking at FDNPP led to the evacuation of the population near the plant and an intense concern in Japan and around the world about the coastal environment and its potential long-term impacts on the Pacific Ocean. The US National Science Foundation (NSF) quickly funded a number of RAPID grants to investigate different aspects of the earthquake, tsunami, inundation, and nuclear disaster (EERI, 2012). An interdisciplinary team of U.S. and Japanese scientists (geophysics, physical and biological oceanography, coastal engineering) was formed to make a model assessment of the March 11 earthquake, tsunami formation and evolution, coastal inundation, and initial spread of the Fukushima radionuclides into the Pacific Ocean (Beardsley et al., 2012).

Several scientific and technical issues arose during an initial stage of our research. First, if only the tsunami was concerned, one could follow a traditional approach to simulate the tsunami using a two-dimensional (vertically-integrated) shallow water

* Corresponding author at: School for Marine Science and Technology, University of Massachusetts-Dartmouth, New Bedford, MA 02748, USA. Tel.: +1 508 910 6388.
E-mail address: c1chen@umassd.edu (C. Chen).

http://dx.doi.org/10.1016/j.pocean.2014.01.002
0079-6611/

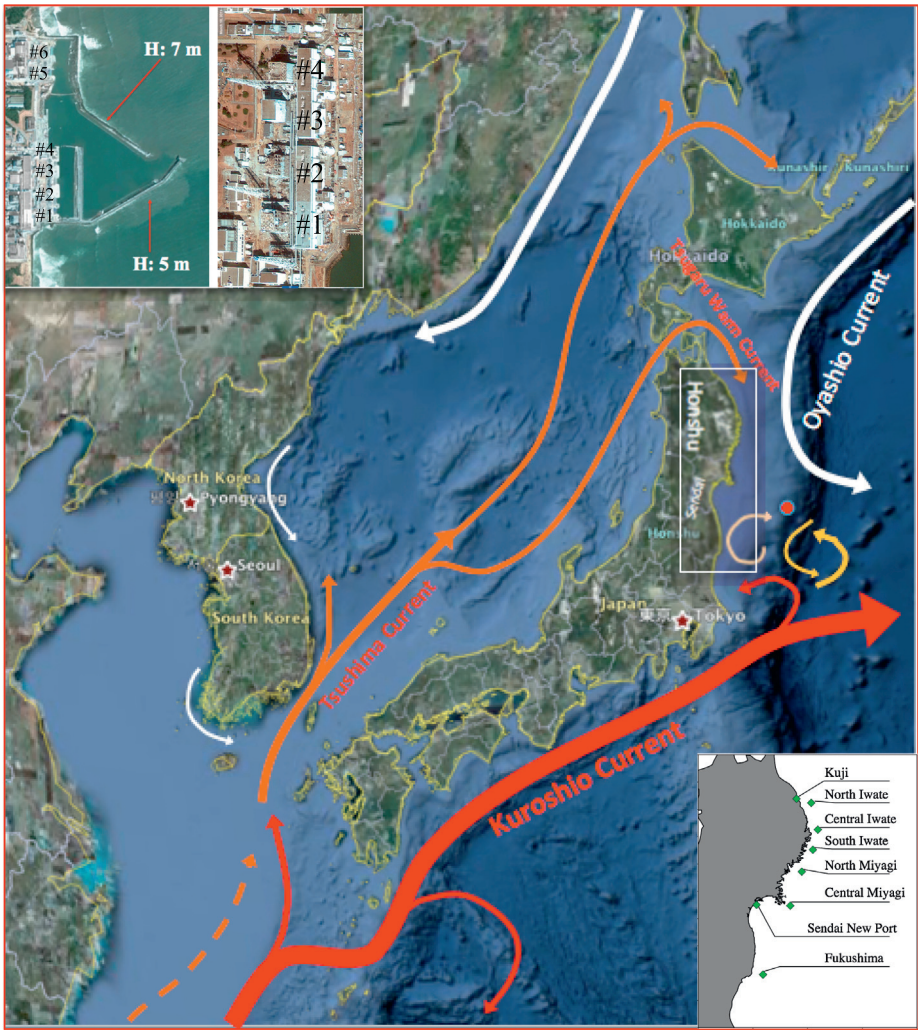

Fig. 1. Location of the mainshock with epicenter at 38.30°N, 142.37°E at 5:46 UTC (local time at 14:46 PM) on March 11, 2011 (USGS, 2011), followed by a M7.9 aftershock on the eastern Japanese shelf (filled red dot); the regional circulation pattern (color vector lines); enlarged view of the Fukushima Dai-ichi Nuclear Power Plant (FDNPP) (upper-left) with heights of breakwaters and an adjacent image showing the damage of FDNPP facilities (downloaded from http://www.nytimes.com/interactive/2011/03/13/world/asia/satellite-photos-japan-before-and-after-tsumami.html); and the locations of eight coastal tide gauge stations from Kuji to Fukushima (green dots) used for the model-data comparisons (right-lower) in the Tōhoku region bounded by the white box. (For interpretation of the references to color in this figure legend, the reader is referred to the web version of this article.)

equation model by specifying the initial sea level change due to the earthquake (e.g., Sasaki et al., 2011, 2012; Kim et al., 2011). For the March 11 Tōhoku earthquake event, however, the inundation produced by the tsunami damaged the FDNPP facility and led to a serious release of radionuclides into the coastal ocean. If one attempted to extend the tsunami simulation to track the spread of radionuclides thereafter, the flow field would be required. A better approach would be to use a three-dimensional (3-D) ocean model capable of resolving the multi-scale barotropic and baroclinic advective processes in the FDNPP-inner shelf and regional ocean complex (Fig. 1). This model should include realistic forcing conditions, not only for the initial perturbation of sea level but also for tidal, wind and buoyancy forcing to simulate the coastal and regional circulation and stratification. After the initial simulation of the March 11 tsunami and coastal inundation, this model could then be used to track the initial spread of radionuclides (esp. Cs-137; half-life ~30 years) from the FDNPP into and across the shelf (Lai et al., 2013). To our knowledge, simulating tsunami waves using a 3-D stratified ocean model has not been tried in the past.

Second, after the earthquake, several seismic rupture models were proposed to examine inversely the geophysical dynamics for this earthquake (Toda et al., 2011). These models were based on seismic, geodetic and tsunami observations. While several modeling efforts were also made to simulate the tsunami waves under idealized initial conditions (e.g. Yoon et al., 2011; Kim et al., 2011; Chan and Liu, 2012), to our knowledge, no assessment has been performed by simulating the tsunami and subsequent coastal inundation using an ocean model with realistic forcing conditions and initial seafloor changes constructued based on multi-sources of measurements at monitoring sites by these seismic models. Such an assessment could provide us with an alternative independent evaluation of these seismic models for their reality and accuracy in presenting the observed features of the tsunami waves and coastal inundation.

Third, scaling analysis suggested that the initial tsunami waves produced by the March 11, 2011 Japan earthquake were low-dispersive, weakly nonlinear long waves since the ratios of water depth to wavelength and of wave amplitude to water depth were much smaller than one (Chan and Liu, 2012). It is unclear if hydrostatic dynamics is sufficient to simulate the propagation and runup of these tsunami waves, particularly over the shelf and near the coast where the tsunami waves could become strongly nonlinear

Please cite this article in press as: Chen, C., et al. The March 11, 2011 Tōhoku M9.0 earthquake-induced tsunami and coastal inundation along the Japanese coast: A model assessment. Prog. Oceanogr. (2014), http://dx.doi.org/10.1016/j.pocean.2014.01.002

as the wave amplitude grows closer to or larger than the local water depth. For a given high resolution grid, running a model with hydrostatic and non-hydrostatic dynamics, respectively, could allow us to examine the relative importance of non-hydrostatic dynamics in the tsunami wave simulation.

Fourth, many efforts have been made on examining the behavior of the tsunami wave runup (e.g. Carrier and Greenspan, 1958; Keller and Keller, 1964; Synolakis et al., 2008; Madsen and Schäffer, 2010; Chan and Liu, 2012). Carrier and Greenspan (1958) derived an analytical solution for a nonlinear wave equation for nonbreaking long waves climbing over a linear slope in an inviscid shallow water ocean. Keller and Keller (1964) considered shallow water waves propagating over a more realistic linear two-slope beach, but their analytical solution was valid only for linear theory. A solution that could be applied for both linear and nonlinear shallow water waves was derived by Synolakis et al. (2008) and Madsen and Schäffer (2010). All of these analytical studies, however, were conducted for idealized 2-D (x–z where x is the cross-isobath direction and z is the vertical direction) canonical problem in which the wave propagated from a constant depth region to the linear slope with no lateral (along-isobath) variation. The central Tōhoku shelf north of the FDNPP is characterized by a concave coastline, and our model simulations of the March 11 Japan tsunami waves exhibited 3-D features as the waves reached the coast. A comparison of our 3-D model simulations with these analytic theories could provide new insight into their applicability and limits.

In addition to scientific issues, intense public attentions have focused on the radionuclides leaking from FDNPP. It is unclear how the tsunami was amplified when it entered the FDNPP facility area from the shelf and how it affected the resulting inundation. The FDNPP facility damage image (Fig. 1) implied that the tsunami seemed higher on the southern side than on the northern side, and more serious on the back rather than on the front. Did the facility breakwaters (designed for a peak wave elevation of 5.0 m) act to influence the flooding around the FDNPP? Since the horizontal resolution and bathymetry used in previous models were too coarse to resolve the near-shore tsunami propagation towards the FDNPP, these questions were not addressed until our studies.

To address these issues, we developed an integrated seismic-ocean-tracer model system to examine the tsunami formation, inundation, and initial spreading of Cs-137. In this paper, we present our key results on the initial tsunami generation, subsequent propagation, and coastal inundation. A subsequent paper (Lai et al., 2013) has investigated in more detail the dynamics controlling the initial pathways of Cs-137 from the FDNPP to the shelf break.

Our model system features a nested global-Japan coastal FVCOM system. Using high-resolution bathymetry and elevation data obtained from the Japan Oceanographic Data Center and Geospatial Information Authority of Japan, the local model domain was configured with a horizontal resolution up to 5 m in regions of complex inner-shelf-land topography and around the FDNPP. Under realistic oceanic conditions that include the Kuroshio, tides and wind forcing, we first conducted experiments with the initial March 11 earthquake bottom movements provided by five advanced seismic rupture models. The seismic models were then evaluated through comparisons of model-simulated sea level with observations at coastal tide gauges and model-predicted inundation areas with inundation maps constructed from field survey results. We next determined the relative importance of non-hydrostatic dynamics on the tsunami wave runup and compared our model results with the analytic runup model solutions.

2. The integrated model system and experiment design

The ocean model used in this study is a global-regional-coastal nested FVCOM system (hereafter referred to as the nested global-Japan coastal FVCOM system) (Fig. 2). FVCOM is a prognostic, unstructured-grid Finite-Volume Community Ocean Model developed originally by Chen et al. (2003) and upgraded by team efforts (Chen et al., 2006a,b, 2013). FVCOM solves the flux form of the

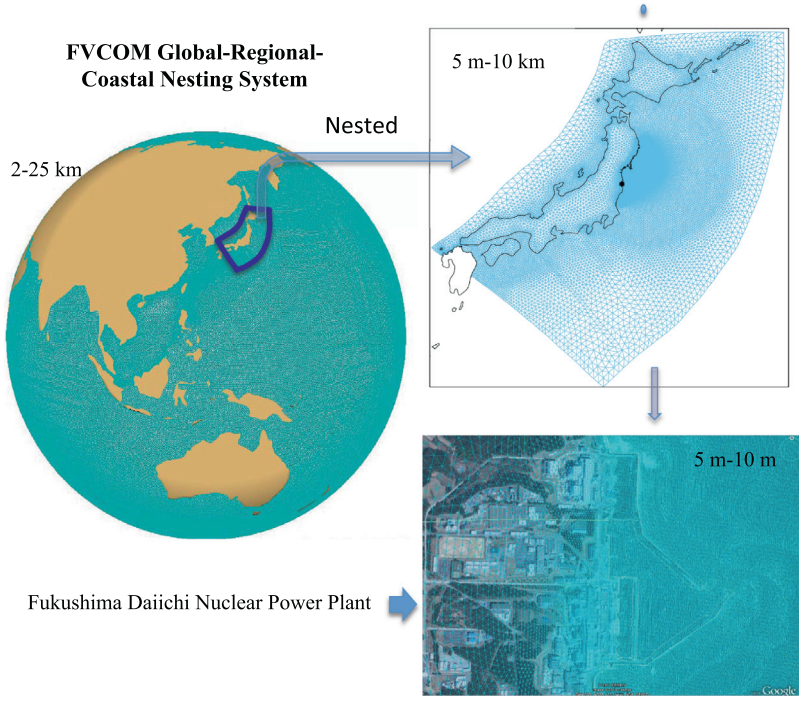

Fig. 2. Illustration of nested Global-JC FVCOM system. Blue line presents the nesting boundary between Global-FVCOM and JC-FVCOM. Left: Global-FVCOM grid; right-upper: JC-FVCOM grid; and right lower: enlarged view of the grid in the FDNPP. The horizontal resolution varies in range of 2–25 km for Global-FVCOM and 5 m to 5 km for JC-FVCOM. (For interpretation of the references to color in this figure legend, the reader is referred to the web version of this article.)

Please cite this article in press as: Chen, C., et al. The March 11, 2011 Tōhoku M9.0 earthquake-induced tsunami and coastal inundation along the Japanese coast: A model assessment. Prog. Oceanogr. (2014), http://dx.doi.org/10.1016/j.pocean.2014.01.002

governing equations in control volumes constructed with multi-triangular meshes using a second-order accurate discrete flux scheme. This model uses an unstructured grid in the horizontal and a terrain-following coordinate in the vertical. The unstructured triangular grid provides a better fitting of irregular coastal geometries and flexibility in adjusting the grid resolution to capture the key physical processes (Chen et al., 2007). The finite-volume approach ensures the conservation of mass, heat, salt, and tracer concentrations in the sense of numerical computation. The latest version of FVCOM (v3.1.6) used in this study is a fully coupled current-wave-sediment-ice model with multiple options for domain nesting, flooding/drying processes, and hydrostatic/non-hydrostatic solvers (Chen et al., 2013). The wet/dry treatment algorithm used to simulate the coastal inundation is described in Appendix A.

The global-Japan coastal nested FVCOM system includes two models: (1) Global-FVCOM and (2) Japan coastal FVCOM (JC-FVCOM). These models are nested through the common boundary cells. Global-FVCOM uses the spherical version of FVCOM to cover the entire global ocean with inclusion of all major rivers (Fig. 2, left panel). Its grid features a horizontal resolution varying from 2 km along Japan's coast to 25 km in the interior. A hybrid terrain-following (s- to sigma-) coordinate system is used in the vertical, with a total of 45 layers, 10 and 5 uniform layers near the surface and bottom, respectively, in regions deeper than 225 m, switching to the sigma-coordinate in continental shelf and coastal regions shallower than 225 m. The thickness of the uniform layers is 5 m, so the hybrid coordinate transition occurs at the location where all layers have uniform thickness of 5 m. This hybrid coordinate prevents numerical errors in the simulation of surface mixed layer and bottom boundary layer dynamics in the interior of the ocean without losing vertical resolution in the shallower coastal regions. Global-FVCOM is driven by (a) astronomical tidal forcing with eight constituents (M_2, S_2, N_2, K_2, K_1, P_1, O_1, and Q_1), (b) surface wind stress, (c) net heat flux at the surface plus shortwave

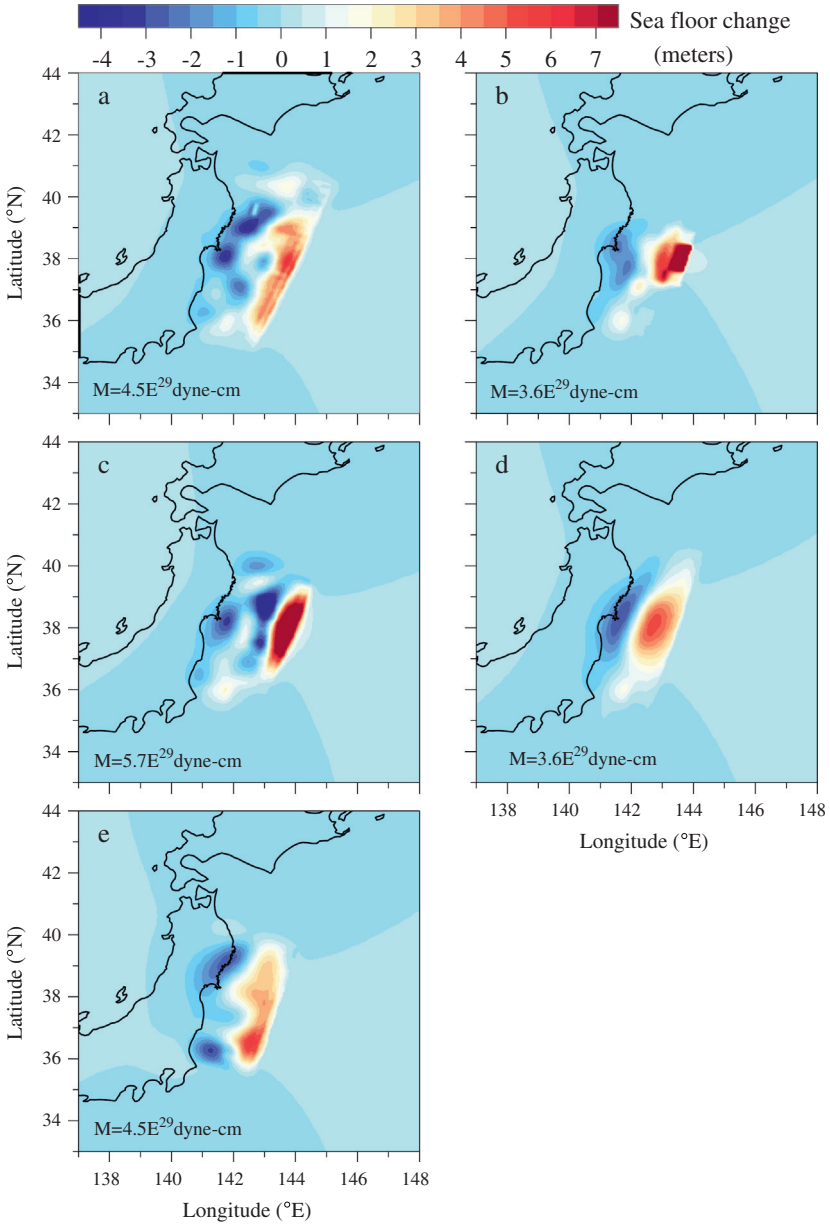

Fig. 3. Seafloor changes estimated based on five seismic rupture models of the March 11 M9.0 mainshock and M7.9 aftershock. Named as case-a for Wei and Sladen (2011) and Simons et al. (2011); case-b for Fujii et al. (2011); case-c for Shao et al. (2011); case-d for Pollitz et al. (2011), and case-e for Yagi and Fukahata (2011).

Please cite this article in press as: Chen, C., et al. The March 11, 2011 Tōhoku M9.0 earthquake-induced tsunami and coastal inundation along the Japanese coast: A model assessment. Prog. Oceanogr. (2014), http://dx.doi.org/10.1016/j.pocean.2014.01.002

irradiance in the water column, (d) surface air pressure gradients, (e) precipitation (P) minus evaporation (E), and (f) river discharge. The external forcings were generated by two sources: (1) global NCEP/NCAR reanalysis data at a 6-h time interval and a 1.88-degree resolution, and (2) regional MM5/WRF reanalysis data at a 1-h time interval and a 10-km resolution. We merged these two datasets together and interpolated into an hourly time interval time series at each grid node. The heat flux was adopted from version 2 of the CORE (Common Ocean Reference Experiment) global air-sea flux dataset. The river discharges were collected from different countries. For the rivers terminating on the US and Canada coasts, the discharge data were downloaded directly from the US USGS website (http://waterdata.usgs.gov/nwis) and the Canadian website (http://www.wsc.ec.gc.ca/applications/H2O/index-eng.cfm). For the regions where no river discharge data were available, we used the climatological data that are used for the Navy global ocean model.

Global-FVCOM has been validated through a 50-year spin-up simulation and a 35-year (1978–2012) hindcast assimilation (http://202.121.64.88:8000/fvcomwms/). An example for the accuracy of the tidal simulation in the western Pacific coastal regions was given in Hu et al. (2012), which suggested that the Global-FVCOM provides the same accuracy as regional tidal models used in that region.

JC-FVCOM was configured with horizontal resolution varying from 5 km near the boundary nesting with Global-FVCOM to 5–10 m in the nearshore coastal region (including the FDNPP) and inland up to a distance of 15 km from the coast (Fig. 2, right panels). JC-FVCOM had the same hybrid vertical coordinate system with 45 layers and was forced with the same meteorological forcing as Global-FVCOM.

For this study, the Global-FVCOM hindcast started on January 1, 2011 with initial conditions provided from the hindcast results of 2010 and continued to July 31, 2011. The M9.0 Tōhoku earthquake struck at 5:46 UTC March 11 with its epicenter near 38.30°N, 142.37°E (USGS, 2011), causing a large change in the bottom bathymetry on the Japan trench mega-thrust area east of northern Honshu Island. Within ~2 min, the bottom elevation over a large area (200 × 500 km) shifted significantly, with a maximum uplift of ~7 m and depression of ~3.5 m. At 6:15 UTC, a major M7.9 aftershock struck near 35.92°N, 141.38°E, causing an additional bottom elevation change in a smaller area near the southern coast. JC-FVCOM started running at 0:00 UTC on March 11, 2011 with nested boundary conditions provided by the Global-FVCOM and sea level changes predicted by five seismic rupture models for the combined M9.0 mainshock and M7.9 aftershock at 5:46 UTC on that day.

The seafloor changes predicted by the five seismic rupture models, which were described in detail in Toda et al. (2011), are shown in Fig. 3. The five cases were named as case-a for Wei and Sladen (2011) and Simons et al. (2011), using data from teleseismic *P*, *SH*, and long period surface waves plus static GPS; case-b for Fujii et al. (2011), using data from DART tsunamigrams and tide gauges; case-c for Shao et al. (2011), using data from similar sources as Wei and Slanden's except no GPS; case-d for Pollitz et al. (2011), using static GPS data; and case-e for Yagi and Fukahata (2011), using data from teleseismic body waves. The seismic moment was defined as $M_0 = \mu DS$, where μ was the shear modulus of the rocks, D was the average slip on the earthquake rupture plane with the fault surface area S, while the earthquake moment magnitude $M_w = \log M_0/1.5–10.73$ (Stein and Wysession, 2003). The M9.0 mainshock plus the M7.9 aftershock yielded seismic moments of 4.5, 3.6, 5.7, 3.6 and 4.5 E^{29} dyne-cm for cases a–e, respectively. The vertical deformation of the seafloor were calculated for the five seismic models and used as the driving force to trigger the simulated tsunami waves. However, the earthquake-induced local crustal deformation along Japan's coastal regions were not included when comparing model predictions with observations.

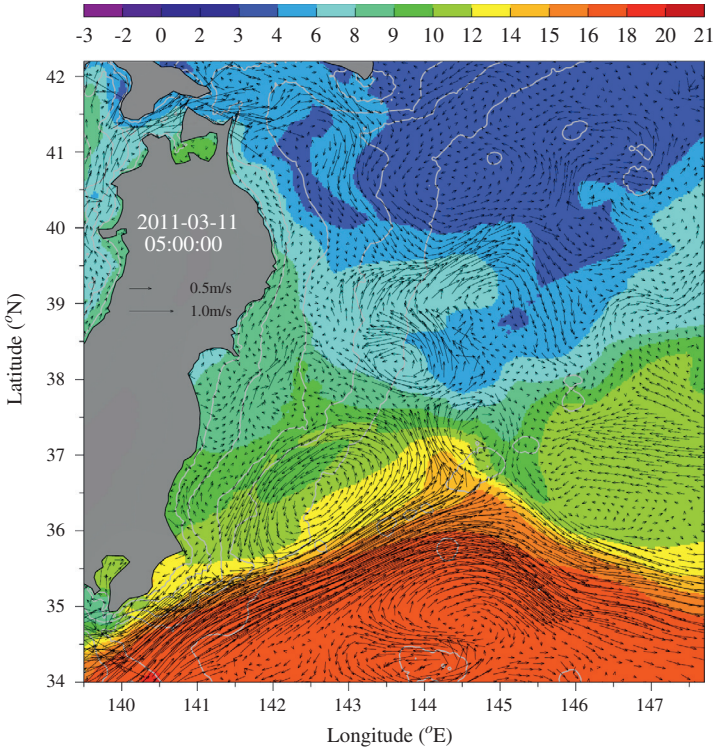

Fig. 4. Distributions of near-surface circulation (vectors) and water temperature (color image) over the Japanese shelf at 5:00 UTC March 11, 2011. The earthquake occurred over the slope and western side of the Japan Trench in a region characterized by strong mesoscale variability of upper-ocean currents between the Kuroshio (on the south) and the Oyashio Current (on the north). At this specified time, the subtidal coastal currents over the shelf were northward.

Please cite this article in press as: Chen, C., et al. The March 11, 2011 Tōhoku M9.0 earthquake-induced tsunami and coastal inundation along the Japanese coast: A model assessment. Prog. Oceanogr. (2014), http://dx.doi.org/10.1016/j.pocean.2014.01.002

The seafloor changes predicted by these five seismic models significantly differed in both magnitude and spatial distributions (Fig. 3). The model-predicted orientations of the major axis of vertical deformation of the seafloor were similar, but case-b and case-c had a much larger vertical deformation than the other three cases. Although case-b and case-c showed the maximum vertical deformation value, case-c covered a larger area than case-b. Case-a showed that there was significant seafloor change north of 40°N, while other cases did not.

At 5:00 UTC, 46 min before the mainshock struck, the surface circulation off northern Honshu Island featured a strong offshore Kuroshio Current on the south with a large cyclonic recirculation centered near 36.5°N, 142.5°E, a small cyclonic eddy centered near 38.3°N, 143.5°E between the Kuroshio recirculation and Oyashio Current, and weaker currents over the continental shelf and upper slope (Fig. 4). The mainshock was centered in a weak current zone between the two cyclonic eddies and occurred near low tide, at which time currents near the coastal region were of order 0.1–0.5 m/s and the prevailing winds were northeasterly with a speed of roughly 5 m/s.

3. Tsunami simulations

JC-FVCOM with initial conditions from the five seismic models was capable of reproducing the tsunami and coastal inundation. As an example, here we use case-a to describe the general features of the tsunami simulations. Fig. 5 shows three snapshots of the distribution of the tsunami waves at 05:51:53, 06:15:03 and 06:42:23 (hours:minutes:seconds) UTC, March 11. The initial leading tsunami wave propagated towards the coast and reached the northern and southern coasts in about 30 min. Large reflections occurred from the northern and southern coasts, turning clockwise on the north and counterclockwise on the south, rejointing the tsunami waves that propagated towards the Miyagi coast. The largest inundation occurred along the Miyagi coast in Sendai Bay, due to both the relatively low and flat land features and the tsunami wave energy accumulation from the reflected waves on both the coasts. The 06:42:23 snapshot clearly showed that the reflected waves tended to push the water from both sides towards the center of the Miyagi coast. The primary wave had an initial phase speed of about 200 m/s and slowed down as the wave propagated across the shelf and towards the coast (Fig. 6). By the time when the primary wave reached the coast, the phase speed was about 30 m/s on the northern coast, 40 m/s on the southern side, and 60–70 m/s in the middle of Miyagi.

The FDNPP is located at 37.42°N, 141.03°E on the southern area of Miyagi coast (Figs. 1 and 6). When the mainshock primary wave entered this facility, it was split into two branches by the northern and southern breakwaters, and the maximum surface water current speed exceeded 27 m/s (Fig. 7), which was two times larger than the maximum currents measured by tsunami video images taken in Kesennuma Bay (Fritz et al., 2012). The breakwaters, designed to protect the nuclear facility from a smaller tsunami, also functioned as a wave guide to increase the water flux onto the northern and southern ends of the facility. The water first flowed onto the southern land and then onto the northern land. The water then retreated back into the facility from land. While much of the water drained back to the ocean after the primary wave, a significant amount of water remained in the inland areas around

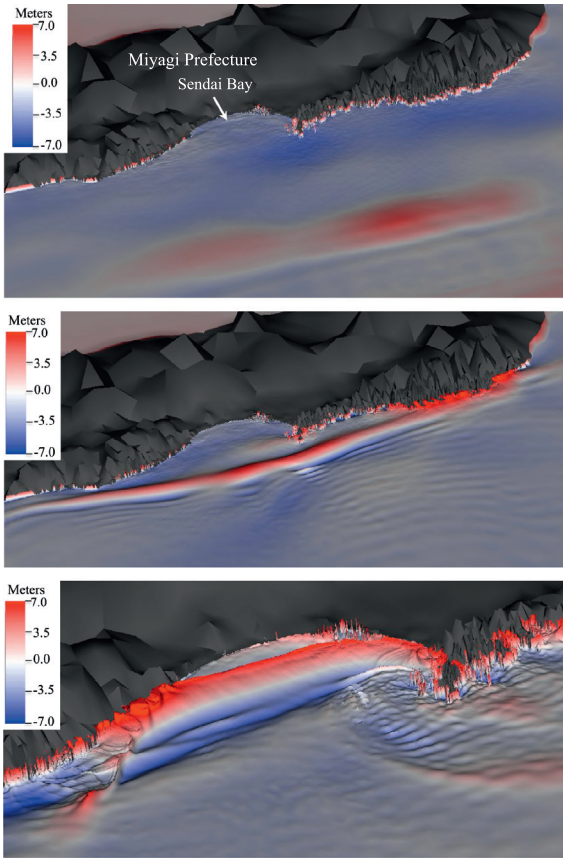

Fig. 5. Snapshots of the water level distribution (m) of the leading tsunami wave over the eastern Japanese shelf at 05:51:53, 06:15:03 and 06:42:23 (hours:minutes:seconds) UTC on March 11, 2011.

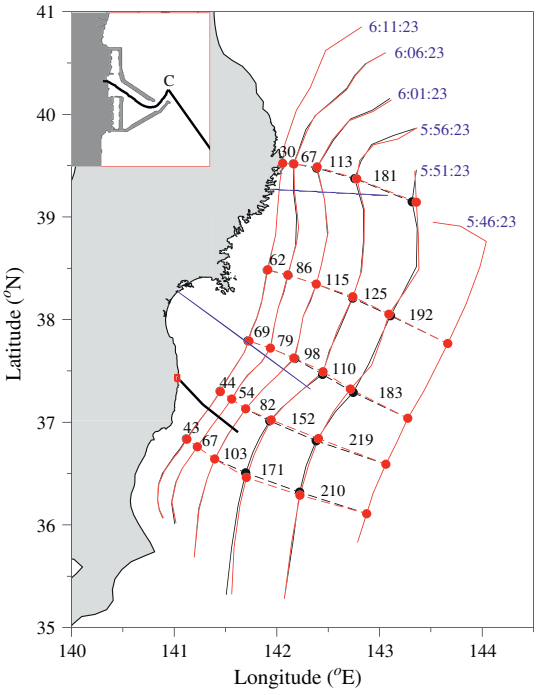

Fig. 6. The distribution of the tsunami peak as it propagated towards the coast on March 11, 2011 (black line: hydrostatic; red line: non-hydrostatic). Black and red dots are the locations where the wave speeds are calculated for hydrostatic and non-hydrostatic cases and values next to the dots are the wave speed values in m/s for the hydrostatic case. The blue number was the time (units: hours:minutes:seconds) at which the tsunami peak was drawn. Heavy black line is the section selected to show the comparison of hydrostatic and non-hydrostatic results as the tsunami approached the FDNNP. The upper right panel is the enlarged view of the area around FDNPP bounded by a red box. Two blue lines indicate the north and south sections used to compare the model-predicted runup with analytical solutions. (For interpretation of the references to color in this figure legend, the reader is referred to the web version of this article.)

Please cite this article in press as: Chen, C., et al. The March 11, 2011 Tōhoku M9.0 earthquake-induced tsunami and coastal inundation along the Japanese coast: A model assessment. Prog. Oceanogr. (2014), http://dx.doi.org/10.1016/j.pocean.2014.01.002

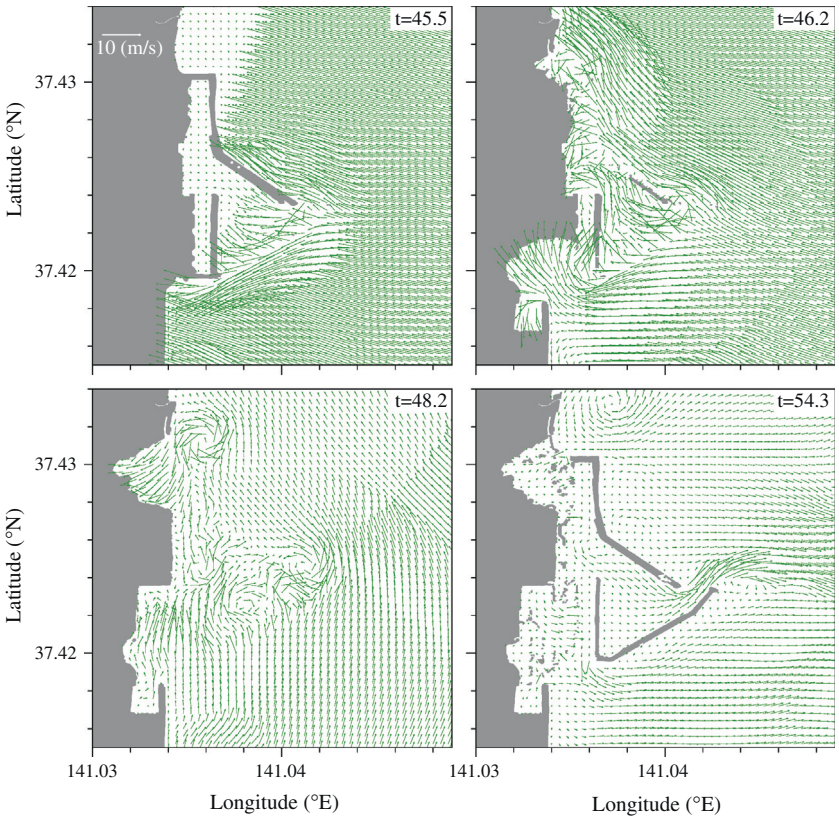

Fig. 7. Distribution of surface water currents before, during, and after the tsunami wave swept over the breakwaters of the FDNPP. The letter "*t*" denotes the time in minutes relative to the time at which the mainshock occurred. The vectors were plotted with a selection radius of 40 m.

nuclear reactors #1–#4 on the south and nuclear reactors #5–#6 on the north. During and after flooding, multiple vortices or whirlpools appeared near and inside the power plant facility areas, with diameters of roughly 50–200 m. During flooding, cyclonic vortices occurred and both cyclonic and anticyclonic vortices were found when the water rapidly retreated back to the ocean.

The larger flooding that occurred on the southern side was a result of the higher sea level on the southern breakwater. We compared the time series of the sea level at site A on the north and site B on the south of the facility (Fig. 8). The model predicted a maximum water level of 16.02 m at site B and 13.59 m at site A, a difference of 2.43 m. The model-predicted inundation processes into the FDNPP were consistent with a satellite image made after the mainshock, which showed large damage in the inland areas of reactors #4 and #3 on the south and reactor #1 close to the middle branch of the intrused water (Fig. 1). The vortices or whirlpools were evident in photos taken during this event as well as in other inundated coastal areas (Kim et al., 2011; Lynett et al., 2012), which was believed to be due to the rip current-driven return water from the land after wave breaking.

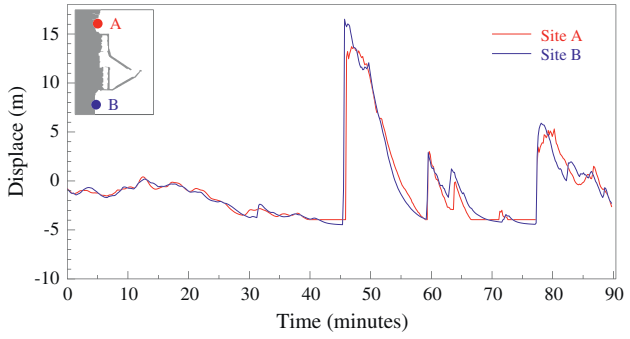

Fig. 8. Time series of the water level at sites A and B (shown in the left-upper panel) during the tsunami.

We compared model-predicted tsunami water levels with measurements from eight tide gauges from Kuji to Fukushima along the eastern Japan coast that experienced significant tsunami damage (Fig. 1). The Kuji gauge failed during inundation so that the maximum water level there was unknown. At Sendai New Port, the measurements showed a peak of 6.65 m. Since the gauge was destroyed a few seconds later, it was unclear if the decrease in water level after that peak was real or caused by instrument failure. The rapid ground geometric deformation caused by the earthquake also caused some measurement errors in amplitude and phase. The uncertainty caused by these errors was not taken into account in the model-data comparisons presented here.

The FVCOM-predicted water levels significantly differed in the five cases even through all cases resolved the main water level peak caused by the mainshock primary wave and subsequent oscillations (Appendix B). The initial condition specified based on case-c was constructed with almost the same data sources as case-a but without GPS. The tsunami intensity, however, was overestimated in case-c and underestimated in case-a, with a better overall results in case-c (Fig. 9). The model predictions for cases a–c captured the peak amplitude and timing better than those for cases d–e (Table 1). At North Iwate, Central Iwate, and South Iwate in the northern area, case-c predicted the water level closest to observations, but the timing was better in case-a at North Iwate and in case-b at Central Iwate and South Iwate. At Central Miyagi, case-a showed the best simulation for water level, and case-b predicted the best timing. At Sendai New Port, all five cases caught the first

Please cite this article in press as: Chen, C., et al. The March 11, 2011 Tōhoku M9.0 earthquake-induced tsunami and coastal inundation along the Japanese coast: A model assessment. Prog. Oceanogr. (2014), http://dx.doi.org/10.1016/j.pocean.2014.01.002

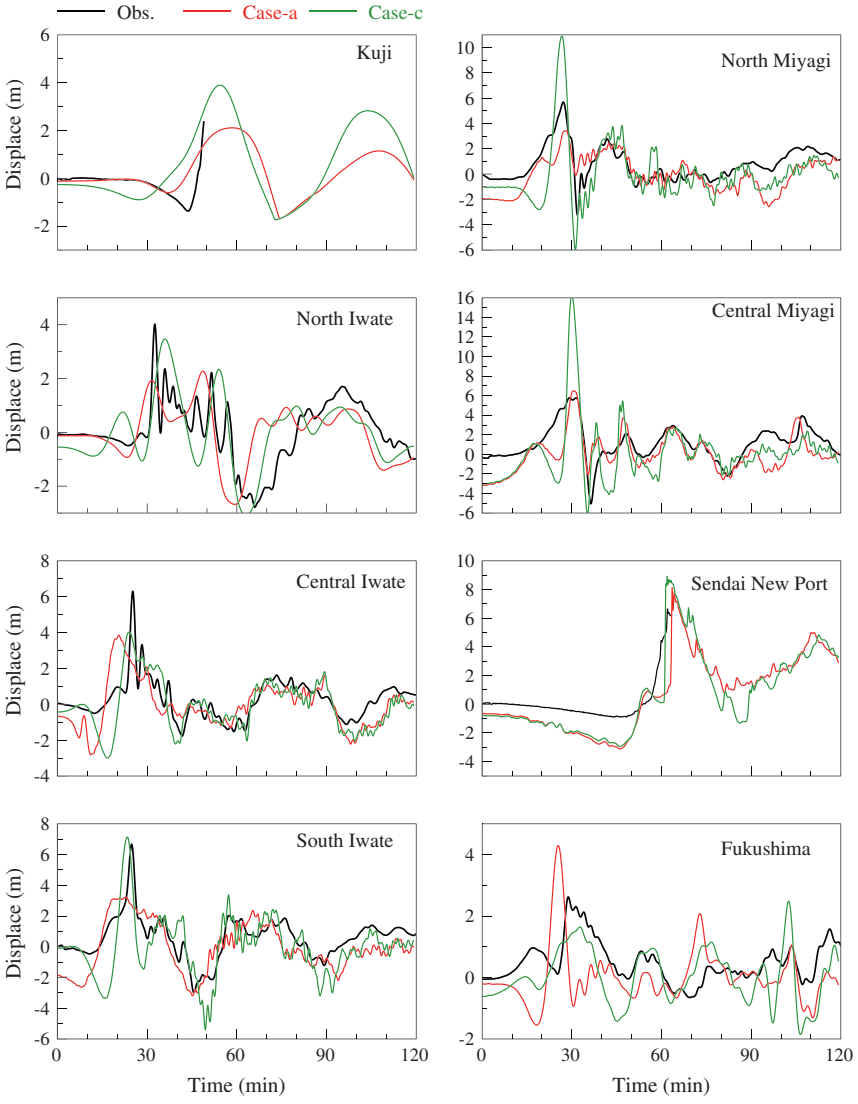

Fig. 9. Comparisons of the model-simulated and observed sea level displacement (m) at eight tide gauges (location shown in Fig. 1) over the initial 120-min period for the model runs with initial conditions of the seafloor change specified by case-a and case-c.

Table 1
Difference between observed and modeled main tsunami peaks and timings for the cases with initial seafloor change calculated using five seismic models.

Station	Case-a		Case-b		Case-c		Case-d		Case-e	
	$\Delta\zeta$ (m)	Δt (min)	$\Delta\zeta$ (m)	Δt (min)	$\Delta\zeta$ (m)	Δt (min)	$\Delta\zeta$ (m)	Δt (min)	$\Delta\zeta$ (m)	Δt (min)
North Iwate	2.09	*1.01*	1.57	−5.59	*0.55*	−3.43	2.41	−5.73	2.67	−7.52
Central Iwate	2.45	4.68	3.01	*−0.97*	*2.27*	1.18	3.84	6.01	4.35	8.65
South Iwate	3.45	2.27	2.86	*0.61*	*−0.46*	1.45	3.87	6.76	3.83	9.58
North Miyagi	2.25	−0.83	1.58	0.69	−5.22	*0.54*	2.79	8.67	2.78	7.12
Central Miyagi	*−0.72*	−1.29	−3.81	*0.38*	−10.54	−0.79	1.70	7.52	4.19	2.85
Sendai New Port	−1.49	−1.52	*−0.10*	−4.35	−2.28	*0.13*	−0.19	1.14	2.31	1.85
Fukushima	−1.67	*3.29*	*0.25*	−4.69	0.98	−3.90	0.69	6.77	−5.35	5.78

Note: Italicized values denote best-fitting models.

largest tsunami peak, not only in amplitude but also in timing. Case-b predicted the most accurate water level, and case-c showed the best timing. If one considered the overall performance based on both water level and phase, case-a was better at this site. At Fukushima, case-b and case-a were the best in amplitude and timing, respectively. These results indicate that the tsunami wave simulation clearly depended on the spatial and temporal distributions of the seafloor change predicted by seismic rupture models. Tsunami simulation results based on an initial condition of idealized seafloor change should be interpreted with caution.

4. Inundation

Configured with 5- to 10-m resolution of the coastal zone bathymetry and land elevation, JC-FVCOM succeeded in reproducing the basic inundation process and flooded areas. The

Please cite this article in press as: Chen, C., et al. The March 11, 2011 Tōhoku M9.0 earthquake-induced tsunami and coastal inundation along the Japanese coast: A model assessment. Prog. Oceanogr. (2014), http://dx.doi.org/10.1016/j.pocean.2014.01.002

model-predicted inundation areas made with the five seismic initial conditions were in reasonable agreement with field survey measurements made by Japanese national and local governments, academic, and other groups (Mori et al., 2011) (Appendix B). For simplicity, we grouped the survey areas into two regions: Region-I, where the most serious inundation occurred (Fig. 10, left panel), and Region-II, the coastal area north of Region-I. We computed the spatial extent of the simulated flooding and compared these areas with those determined by both ground and satellite-based measurements (Table 2). In Region-I, cases a–d showed better agreement with measurement than case-e, with the closest agreement obtained in case-c. The model-measurement difference was about 4–6 km^2 for cases a–b and d, only about 1.9 km^2 for case-c, but about 12.5 km^2 for case-d. These differences, for example, could be identified in Fig. 10 for case-a. Region-II covered the more rugged area north of Central Miyagi, which included several rivers. In this region, the inundation area was significantly overestimated by 1.7 km^2 (about 38%) in case-c and considerably underestimated by 1.6 km^2 (about 36%) in case-e. Case-a, case-b, and case-d showed similar performance, with the closest agreement seen in case-a (~15% underestimated). Cases a–d all were capable of reproducing the inundated spots, but the model-predicted areas at these spots differed from measurements, particularly in the inland areas of the rivers. This was partially due to the relatively lower accuracy of the coastal zone bathymetry and land elevation in these areas and decreased grid resolution along this northern shore, while it was clear that the extent of the predicted flooding was affected by the initial conditions specified by the five seismic models. This result was consistent with the water level comparisons described in Section 3.

The model results for all five cases reproduced accurately the flooded areas in and around the FDNPP (Table 2). Except in case-d, the inundated areas simulated in the other four cases were very close to the measurements, both in spatial distribution and boundary location. An example is shown in Fig. 10 (right panel) for the comparison of case-a and measurements. The major inundation areas measured on the northern and southern regions of the facility were consistent with the tsunami simulation results that a significant fraction of the primary tsunami wave water transport was forced by the breakwaters to flow around the FDNPP and subsequently flood the land on both sides and behind the facility.

Table 2
Comparison between model-predicted and measured inundation areas.

Types	FDNPP (km^2)	Region-I (km^2)	Region-II (km^2)	Sum (I and II) (km^2)
Measured	0.04	32.89	4.47	37.35
Case-a	*0.04*	26.99	3.77	30.76
Case-b	0.03	28.94	3.42	32.36
Case-c	*0.04*	*30.99*	6.15	*37.14*
Case-d	0.03	26.87	*3.51*	30.38
Case-e	*0.04*	20.39	2.88	23.52

Note: Region-I is located within longitudes from 140.84°E to 141.55°E and latitudes from 37.82°N to 38.6°N. Region-II is located within longitudes from 141.47°E to 142.12°E and latitudes from 38.74°N to 39.75°. Italicized values denote best-fitting models. Case-c provides the best overall fit with the combined measurements.

5. Contributions of non-hydrostatic dynamics

We have examined the importance of non-hydrostatic dynamics in the March 11 2013 Japan tsunami wave simulation. No significant difference was observed for amplitude and propagation speed of tsunami waves between hydrostatic and non-hydrostatic

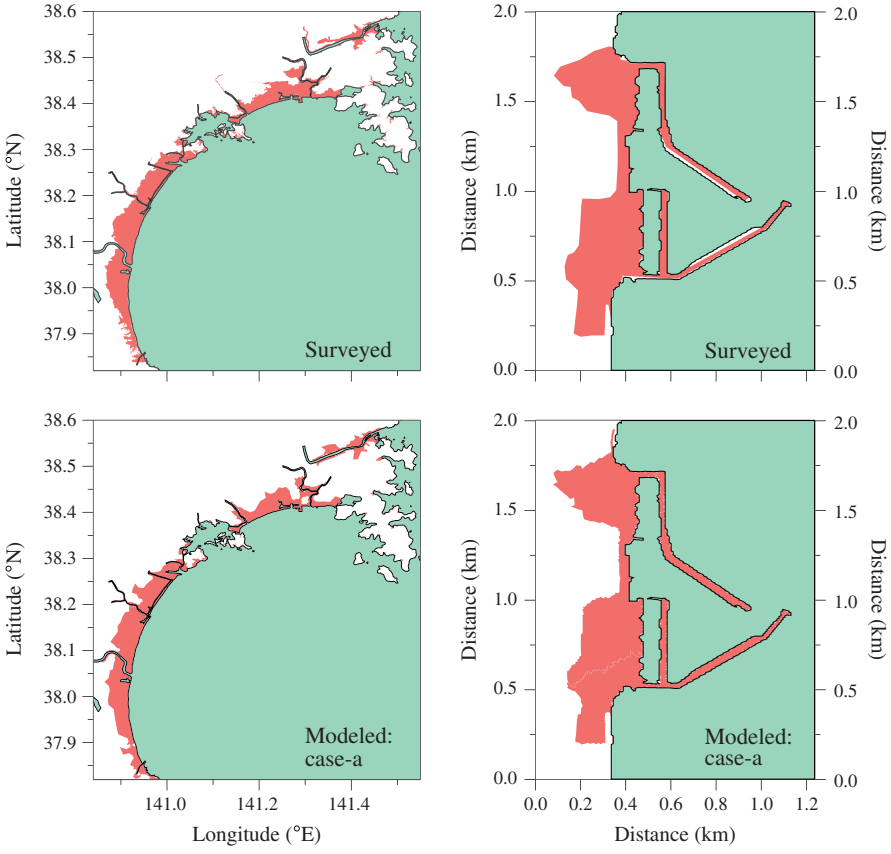

Fig. 10. Comparisons of model-predicted inundation areas with the surveyed areas along the Miyagi coast (left panels) and in the FDNPP region (right panels) for the initial conditions of seafloor change specified by case-a.

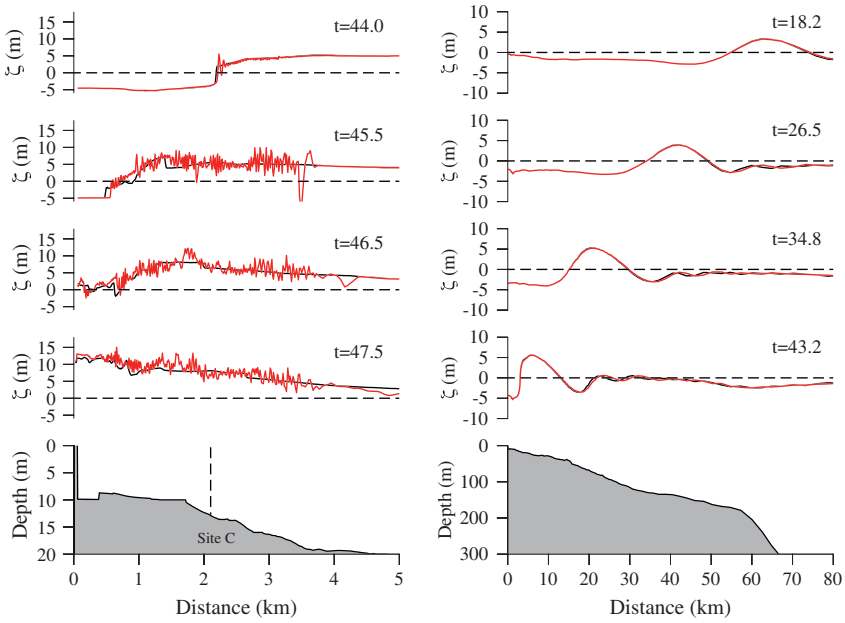

Fig. 11. Comparisons of snapshots of surface elevations (m) predicted by hydrostatic (black) and non-hydrostatic model runs at eight selected times relative to the time at which the mainshock occurred. The letter "*t*" denotes the time in minutes. Water depth (m) along the transect is shown in the bottom panel. The label "Site-C" indicates a location near the breakwater of FDNPP shown in Fig. 6.

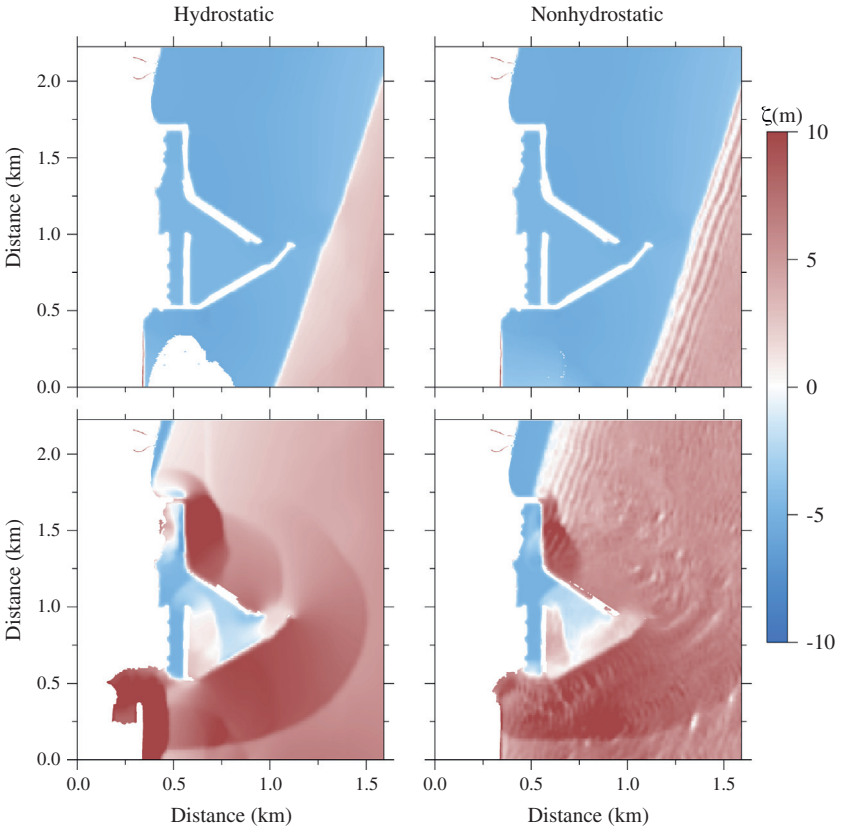

Fig. 12. Distributions of the surface elevation (m) around the FDNPP region at two selected times before the inundation occurred for hydrostatic (left panels) and non-hydrostatic (right panels) cases.

experiments until the waves arrived in regions shallower than ~10 m or less (Figs. 6 and 11). An example can be seen in Fig. 11 for the series of snapshots of surface elevation taken on a transect starting over the shelf and ending at the FDNPP (shown as heavy black line in Fig. 6). The surface elevations simulated by hydrostatic and non-hydrostatic FVCOMs were almost identical over the shelf until the waves reached site-C (shown in Fig. 6) outside of the water passage between the two breakwaters of FDNPP.

Please cite this article in press as: Chen, C., et al. The March 11, 2011 Tōhoku M9.0 earthquake-induced tsunami and coastal inundation along the Japanese coast: A model assessment. Prog. Oceanogr. (2014), http://dx.doi.org/10.1016/j.pocean.2014.01.002

The non-hydrostatic effect started as a vertical perturbation at the crest of the leading tsunami wave at around 44 min after the earthquake, and then developed into a high-frequency wave packet over a few minutes. The high-frequency wave train overlapped over the hydrostatic surface elevation with a wider covering range extending to the backside of the wave crest. This feature was believed to be due to reflection, since it was very close to and inside the area bounded by the breakwaters. Non-hydrostatic processes resulted in a relatively large high-frequency variation (up to a few meters) of surface elevation, but did not change the general flooding tendency as that found in the hydrostatic case. The difference between the hydrostatic and non-hydrostatic tsunami waves can be clearly seen in snapshots of the top-viewed distributions of surface elevation and near-surface current in Figs. 12 and 13. The leading tsunami wave propagated as a water "wall" towards FDNPP in the hydrostatic case, while featuring a wave packet in the non-hydrostatic case. The distributions of the near-surface currents remained similar in these two cases, but the currents in the non-hydrostatic cases exhibited significant spatial variability. Due to the high-frequency fluctuation of surface elevation, timing of the maximum flood onto FDNPP was delayed by a few seconds in the non-hydrostatic case than in the hydrostatic case.

These model results indicated that non-hydrostatic dynamics became important in the region where the water depth was ~10 m or shallower. In this region, the amplitude of the tsunami wave was about 5 m or higher. This was consistent with scaling analysis results, which suggested that over the shelf where the ratio of wave amplitude to water depth was much smaller than one the tsunami was a low-dispersive, weakly nonlinear long wave, and nonlinearity and non-hydrostatic dynamics only became critical in the shallow region where this ratio was O(1).

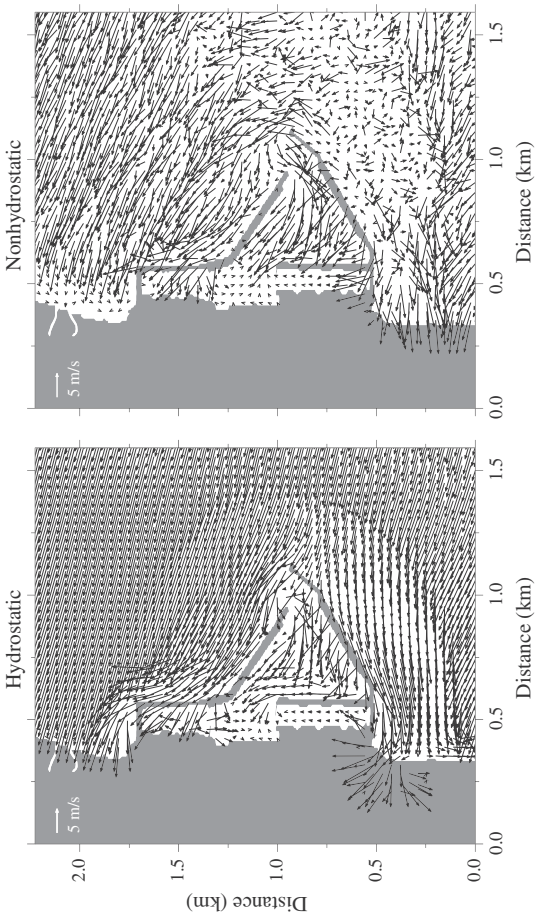

Fig. 13. Snapshots of the distributions of near-surface currents when the leading tsunami wave swept over FDNPP areas for hydrostatic (left panel) and non-hydrostatic (right panel) cases. The velocity scale is shown in the upper left of each panel.

6. Impact of tsunami on vertical mixing

As explained in the introduction, one advantage of using the nested 3-D global-coastal ocean model system is that it has already simulated the regional circulation and stratification, which is a perquisite for tracking radionuclides from FDNPP. Since the tsunami was a solitary-type wave with fast propagation speed (much greater than the ambient currents) and reached the coast in roughly 0.5–1 h, the regional circulation was unlikely to have a significant impact if only the tsunami wave and coastal inundation were considered. To verify this point, we ran JC-FVCOM by removing stratification and wind- and tide-driven circulation. The sea level predicted by this barotropic case at tidal gauges was almost identical to the stratified case during the time before and when the peak of the tsunami wave arrived. A difference in the range of 0.1–1.0 m appeared in the subsequent oscillation period after the leading

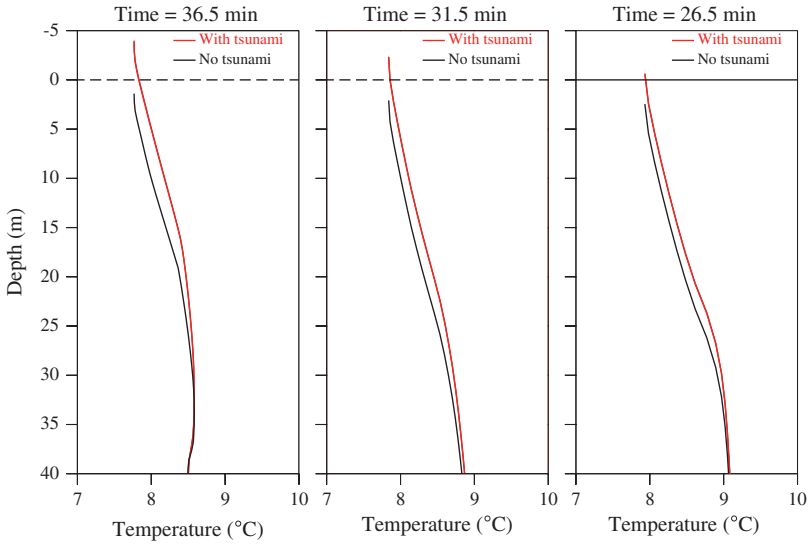

Fig. 14. Vertical profiles of sea temperature (°C) at locations of the tsunami peak 26.5, 31.5 and 36.5 min after the earthquake happened for the cases with (red) and without (black) the tsunami. (For interpretation of the references to color in this figure legend, the reader is referred to the web version of this article.)

Please cite this article in press as: Chen, C., et al. The March 11, 2011 Tōhoku M9.0 earthquake-induced tsunami and coastal inundation along the Japanese coast: A model assessment. Prog. Oceanogr. (2014), http://dx.doi.org/10.1016/j.pocean.2014.01.002

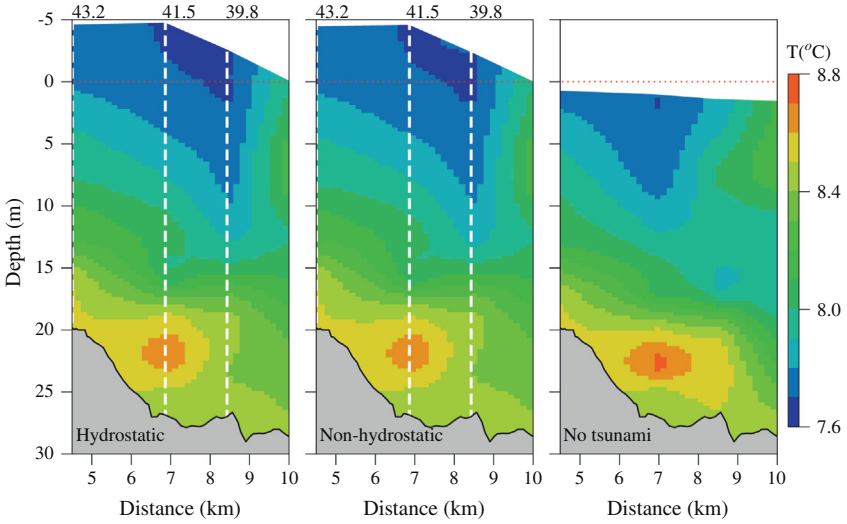

Fig. 15. Temperature sections (°C) at the times 39.8, 41.5 and 43.2 min after the mainshock occurred for the cases without tsunami (right panel) and with the tsunamis predicted by non-hydrostatic (middle panel) and hydrostatic (left panel) models. Heavy white vertical lines in the center and left panels indicate the tsunami peak location at the first two times; the tsunami peak at the third time is located at the left side in these two panels. The values on the top are the time in minutes after the mainshock happened.

tsunami wave landed. This implied that the background circulation and tides could have influences on the tsunami oscillations caused by energy reflection after the leading tsunami wave arrived. We also compared the model-predicted inundation areas for the cases with and without inclusion of stratification. For example, for case-a forcing conditions, the barotropic case predicted a slightly larger inundation area (up to 10%) than the stratified case. Since this difference varied with locations and was also related to initital conditions of the seafloor change in cases a–e, whether or not the background regional circulation and stratification should be included in simulations of the tsunami wave and inundation depends on what level of accuracy one would expect for the tsunami wave simulation.

We did examine how the tsunami wave affected vertical stratification and mixing in our 3-D simulations. In the continental shelf region, the tsunami behaved like a small-amplitude weakly-nonlinear wave. When the leading wave passed, the local vertical temperature profile in the upper 40 m showed a shift of ~0.1–0.2 °C (Fig. 14). This shift had a maximum near the surface and decreased with depth, which was believed due to Stoke's drift. This shift, however, did not change the vertical stratification and thus mixing. The situation was different in the shallow region where vertical mixing was considerably enhanced during the arrival and passage of the leading wave. In this region (Fig. 15), the ratio of wave's amplitude to local depth is O(0.25). While the water column was lifted up, the mixing layer thickness (measured by a temperature range of 7.6–7.8 °C) significantly increased by ~3–5 m in a few seconds. The fact that the near-surface water was colder in the tsunami case implied that the wave intended to wrap the cold water onto the shelf. In Fig. 15, the colder water on the transect appeared at 39.8 min but not at a previous time, suggesting that this wrapping process happened as a 3-D feature. Similar vertical temperature profiles found in the hydrostatic and non-hydrostatic cases were consistent with the results shown in Section 5, where non-hydrostatic effects were negligible until the ratio of wave amplitude to local depth increased to O(1).

7. Comparisons with analytical solutions

We compared the model-predicted runup of the tsunami waves with analytical solutions of solitary waves and so-called *N*-waves. Synolakis (1987) considered the runup of a $\mathrm{sech}(\cdot)^2$ -profile solitary wave propagating from a constant depth region onto a linear slope region and derived a maximum runup law given as

$$R(t) = 2.831 d(\cot\beta)^{\frac{1}{2}}\left(\frac{H}{d}\right)^{\frac{5}{4}} \tag{1}$$

where $R(t)$ is the maximum runup, d is the local water depth, β is the slope angle, and H is the initial solitary wave amplitude. Following Madsen and Schäffer (2010)'s analytical solution and assuming the incident wave was composed of the combination of multi $\mathrm{sech}(\cdot)^2$-profile waves, Chan and Liu (2012) obtained the *N*-wave solution for the maximum runup $R(\tau)$ given as

$$R(\tau) = \sum_{n=1}^{N} R_n^0 Li\left(-\frac{3}{2}, -e^{2\theta_n}\right) - \frac{U^2}{2g} \tag{2}$$

where N is the total number of sech $(\cdot)^2$-profile initial waves, $R_n^0 = 8H_n(2\pi\Omega_n t_o)^{\frac{1}{2}}$, Li () is the Jonquièrès function, $\theta_n = \Omega_n(\tau - t_n - 2t_o)$, U is the velocity given as $U(\tau) = \sum_{n=1}^{N} \frac{2\Omega_n}{s} R_n^0 \mathrm{Li}(-\frac{5}{2}, -e^{2\theta_n})$, $\tau = t - \frac{U(\tau)}{sg}$, s is the beach slope, Ω_n is the nth wave frequency, t_n is the arbitrary phase shift, $t_o = \frac{h_o}{s\sqrt{gh_o}}$, h_o is the local water depth, and g is gravity. For the same initial wave amplitude from the model, we compared the model-predicted maximum runup with analytical solutions (1) and (2) on the two selected sections shown in Fig. 6 (blue lines), and an example for the case-a simulation is shown in Fig. 16.

On the north section, the bottom topography changed from 2000 m to a few meters over a distance of 100 km. This topography could be fitted well by a linear slope with a ratio of 1:46.32 (~0.02). Given an initial incident wave amplitude of 1.0 m, the model-calculated runup agreed very well with the *N*-wave solution. The runup predicted by the solitary wave solution (2) matched well with both model-calculated and N-wave solution-derived values in the region with water depth ⩾200 m, but significantly underestimated the maximum runup (up to a value of 2.5 m) as the wave crossed the shallower region near the coast (For this comparison, the *N*-wave runup was calculated with $N = 1$, which was based on the fact that the solution with $N = 1$ remained the same maximum wave height as the solution with $N > 1$ (Chan and Liu, 2012)). The north section was close to South Iwate. Chan and Liu (2012) compared solutions of solitary waves and

N-waves with runup observed at the TM1, TM2 and South Iwate stations (note: the locations of TM1 and TM2 are almost on a cross-isobath transect from South Iwate, see Fig. 1). By adjusting wave parameters, the *N*-wave solution reasonably matched the observations. Due to poor matching of the time series of surface elevation observed at South Iwate by solitary wave solution, Chan and Liu (2012) demonstrated that the March 11 2011 Japan tsunami was not a solitary wave. Our comparison result on the north section was consistent with their finding, and suggested that on this north section, for a given initial tsunami wave amplitude, *N*-wave theory was capable of capturing the runup process like our 3-D primitive equation model.

On the south section, however, the model-calculated runup significantly differed from both solitary wave and *N*-wave solutions. This section cut across the center of the concave Miyagi shelf, on which the bottom depth changed from 1000 m to a few meter over a distance of 160 km (mean slope ~0.0063). The change of bottom depth with distance was not linear, with a slope of ~0.0097 over

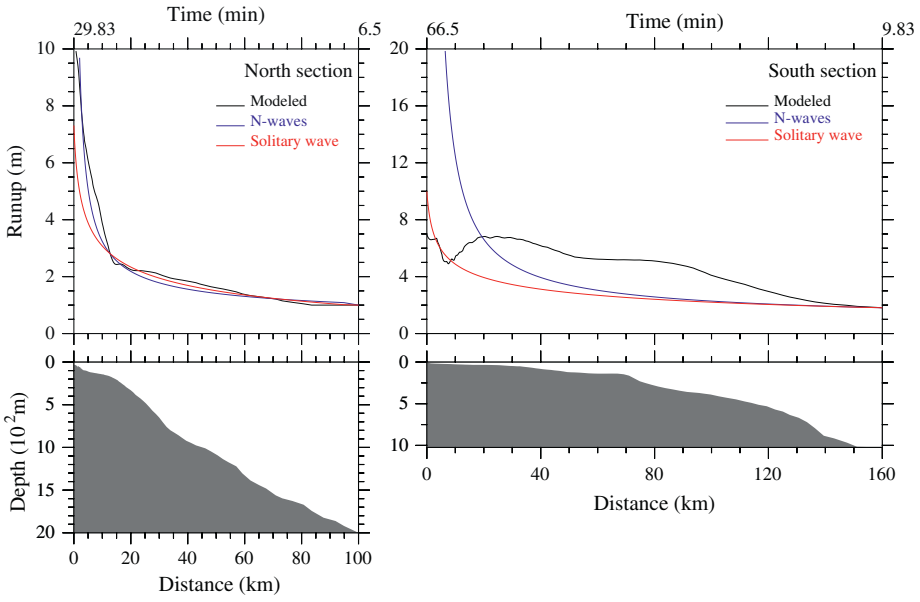

Fig. 16. Comparisons of the model-predicted runup (black) with solitary wave (red) and *N*-wave (blue) analytical solutions on the north section (left panels) and south section (right panels) shown as blue lines in Fig. 6. The bottom panels show the water depth in units of 100 m. (For interpretation of the references to color in this figure legend, the reader is referred to the web version of this article.)

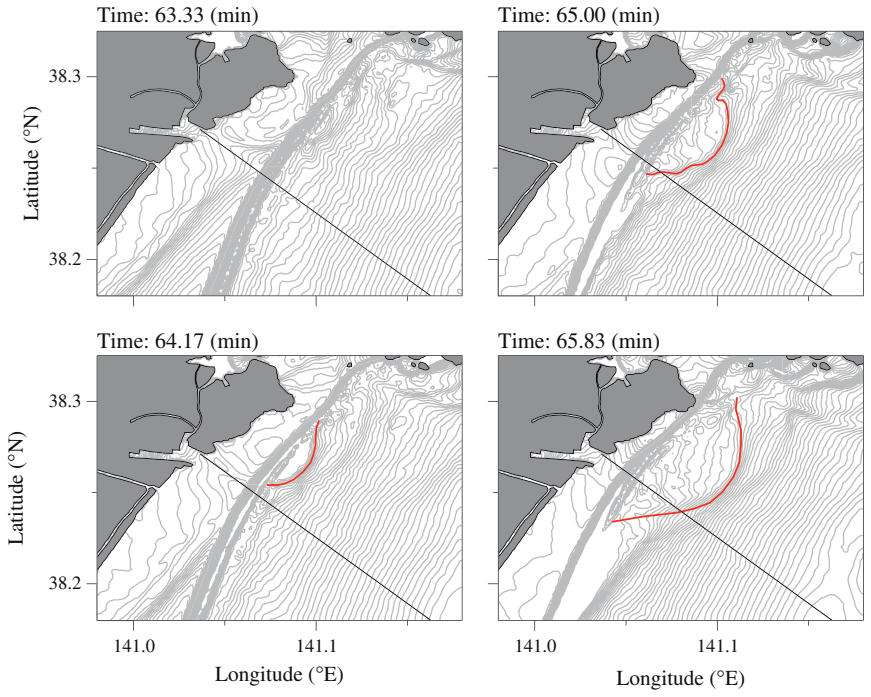

Fig. 17. Snapshots of the surface elevation near the Miyagi coast at the times of 63.33, 64.17, 65.00 and 65.83 min after the mainshock occurred. *Note:* The high gradient contours seen in all snapshots in the region between land and sea are caused by the interpolation program and are not real. The red curves in the last three panels indicate the boundary of the reflected wave-induced relative uniform elevation zone. (For interpretation of the references to color in this figure legend, the reader is referred to the web version of this article.)

Please cite this article in press as: Chen, C., et al. The March 11, 2011 Tōhoku M9.0 earthquake-induced tsunami and coastal inundation along the Japanese coast: A model assessment. Prog. Oceanogr. (2014), http://dx.doi.org/10.1016/j.pocean.2014.01.002

the distance between 70 km and 160 km and ~0.0021 from 70 km to the coast. These slopes were about 2.1 and 9.5 times smaller in comparison with the north section, respectively. Given an initial incident wave amplitude of 1.8 m from the model-computed wave height at 160 km, the analytical solutions showed that a significant increase of runup when the wave arrived in the shallow region with water depth <100 m. The maximum runup at the coast was 10 m for the solitary wave solution but exceeded 20 m for the *N*-wave solution. With the same initial wave amplitude, the model-predicted runup remained higher than the analytical solutions from the initial location to the shelf about 30 km away from the coast. The maximum difference was in a range of 2–3 m. When the tsunami wave arrived near the coast, the wave height dropped from 7 m to 5 m and then increased again to 7 m before the inundation occurred. In this region, the model-predicted runup was significantly lower than the analytical solution.

The difference between the model and analytical solutions could be interpreted by two reasons. First, the analytical solutions were derived using 2-D theory, but it was clear that the tsunami wave in this concave-geometric shelf region was a 3-D feature with energetic wave reflection from both northern and southern coasts (Fig. 5). The higher wave height predicted over the shelf by the model was believed to be due to the reflection energy, a process not included in the 2-D solutions. Second, the analytical solutions were derived on an assumption of a linear bottom slope. This assumption seemed to fit well on the north section but not on the south section. Also, the reflection occurred after the tsunami arrived on the northern and southern coast, which helped explain why the model matched the *N*-waves' solution well on the north section but not on the south section.

Our model showed that on the south section, runup dropped before the tsunami landed. This feature was also related to wave reflection, which occurred over the shelf due to the concave coastline. The effect of wave reflection around that period is clearly shown in Fig. 17. At 63.33 min after the earthquake, the leading tsunami wave arrived in the shelf region about 25 km away from the coast, where the wave height reached ~7 m (Fig. 16). Since the tsunami had arrived on the northern part of the coast at this time, energy there was reflected and extended southward just on the back of the leading wave (Fig. 17). The effected area grew rapidly southward in about 2.5 min, which tended to homogenize the wave height around the wave crest (Fig. 17). This was the cause for the drop of the runup before the leading tsunami wave landed. When the leading tsunami wave was close to the coast, the runup increased again before the inundation started.

8. Discussion and conclusions

Our experiments have demonstrated that the nested global-Japan coastal FVCOM system was capable of simulating the March 11, 2011 Tōhoku tsunami and coastal inundation. By running the ocean model using the seafloor change predicted by five different seismic rupture models as initial conditions, we provided an alternative oceanic evaluation of these seismic models. Key findings from this "forward" simulation approach are summarized as follows. First, for the given same ocean conditions, these seismic models were capable of reproducing the main features of the tsunami and coastal inundation. However, the degree of agreement between the FVCOM-predictions and observations varied significantly with the five different initial conditions. Second, the fact that case-c with the highest seismic moment showed the best overall simulation in both water level and spatial extent of coastal inundation implied that the moment of these seismic models was a factor that could influence the ocean model simulation. However, this factor was certainly not the controlling parameter since case-e had the same moment as case-a, but its performance was not as good as case-a. Also, case-b's moment was much lower than case-c and case-a, but its performance was similar to case-a. Third, our experiments suggested that including more data into the seismic rupture model did not always provide a better solution. Case-c was developed with almost the same data sources as case-a but without GPS. The tsunami intensity was overestimated in case-c and underestimated in case-a, but case-c provided a better overall result. Finally, the seismic rupture models based on multiple monitoring data sources have been widely used to study earthquake dynamics. Coupling seismic models with an ocean model could provide an alternative tool to evaluate these seismic models and also enhance our understanding of the possibility and reality for rapid prediction of a tsunami after an earthquake.

The good agreement of the model-simulated inundation areas with observations demonstrated that with better resolution of coastal geometry for a given accurate local bathymetry, an unstructured-grid nested-domain ocean model was capable of reproducing the March 11, 2011 Japan tsunami and resulting coastal inundation. Significant differences in sea level and inundation areas were found in the model-data comparisons, which suggested that it was critical to capture the seismic moment of the earthquake and spatial distribution of the seafloor change if one intended to use an ocean model to predict the tsunami and flooding. With sufficient spatial resolution around the FDNNP facility, the model accurately predicted the flooding observed at the facility and identified the key role of the breakwaters in the flooding process.

The comparison of hydrostatic and non-hydrostatic experiment results indicated that the March 11 2011 Japan tsunami was a weakly nonlinear long wave as it propagated from its origin towards the coast. Non-hydrostatic effects became a critical factor in the shallow region where the amplitude of the leading tsunami wave grew to the same order of the local water depth. In this case, the transition depth was about 10 m or shallower.

The initial tsunami wave developed 3-D features as it approached the Miyagi shelf caused by wave reflection from the northern and southern coasts. The model-simulated runup matched well with the *N*-wave analytical solution on the northern shelf where the bottom topography featured a linear slope, but not in the concave Sendai Bay where the bottom topography was complex and effects of wave reflections from northern and southern coastal regions were significant. Using 2-D analytical solutions to interpret this tsunami event needs to be viewed with caution.

In the continental shelf region where the wave amplitude was much smaller than local water depth, the arrival and passage of the initial tsunami wave caused little change in the vertical stratification and essentially no mixing in both the hydrostatic and non-hydrostatic experiments. This changed as the ratio of wave amplitude to local water depth grew to about 0.25 or greater, thereafter significant mixing occurred. The effect of this change in stratification on the near-shore currents and their role in the initial spread of radioactivity from the FDNPP was discussed in Lai et al. (2013).

Acknowledgements

This project was supported by US NSF RAPID Grants #1141697 and #1141785 and the JST J-RAPID Program. The development of Global-FVCOM was supported by NSF Grants ARC0712903, ARC0732084, and ARC0804029. We would like to thank J. Qi at the Marine Ecosystem Dynamics Laboratory for the development of multi-domain nesting modules in FVCOM, and P. Xue, G. Gao, Q. Xu and Y. Zhang for their assistances in converting the results into animations. C. Chen, R. Ji and H. Lin's contribution is also supported by the International Center for Marine Studies at Shanghai Ocean University through "Shanghai Universities First-class Disciplines Project".

Please cite this article in press as: Chen, C., et al. The March 11, 2011 Tōhoku M9.0 earthquake-induced tsunami and coastal inundation along the Japanese coast: A model assessment. Prog. Oceanogr. (2014), http://dx.doi.org/10.1016/j.pocean.2014.01.002

Appendix A. The FVCOM wet/dry point treatment Algorithms and validations

One of the most difficult problems in the coastal inundation modeling is to provide an accurate simulation of the water transport flooding onto and draining out of the land. In the last three decades, two types of approaches have been developed to solve this issue: one is the moving-boundary method and the other is the wet/dry point treatment method. In the first method, the computational domain is bounded by an interface line between land and water where total water depth and normal transport are equal to zero (Lynch and Gray, 1980). Because this boundary moves over flooding and draining cycles, the model grid must be re-generated at every time step. This method seems to work for idealized estuaries and coasts with simple geometries (Sidén and Lynch, 1988; Austria and Aldama, 1990), but it is not easy for application to realistic coastal regions with complex geometry including tidal creeks, islands, barriers, and inlets. In the second method, the computational domain covers the maximum flooding area. Numerical grids consist of wet and dry points with a boundary defined as an interface line between water and land respectively. The wet and dry points are distinguished by the local total water depth of $D = H(x, y) + \zeta(x, y, t)$ (where H is the reference water depth and ζ is the surface elevation). The wet point is a grid point with $D > 0$, otherwise, $D = 0$ at dry points. At dry points, velocities are automatically specified as zero, but salinity retains the same value from the previous time step. Since this method is relatively simple, it has been widely used to simulate the water transport over inter-tidal areas in estuarine models (Leendertse, 1970 & Leendertse, 1987; Flather and Heaps, 1975; Ip et al., 1998; Zheng et al., 2003, Chen et al., 2008c).

The wet/dry point treatment technique works only for the case in which a finite-value solution of the governing equations exists as D approaches zero. In a z-coordinate system, to ensure numerical stability of a 3-D model, the thickness of the layer closest to the surface must be greater than the amplitude of the tidal elevation (Davies et al., 1997). This makes it difficult to apply this method for a shallow estuary in which the amplitude of the tidal elevation is the same order of magnitude as the local water depth. Because irregular bathymetry is poorly resolved in a z-coordinate model, it is not likely that the water transport can be accurately simulated over realistic bathymetric inter-tidal zones during both flooding and draining periods. Examples of the z-coordinate wet/dry methods can be seen in Casulli and Cheng (1991, 1992) and Casulli and Cattani (1994), and Hervouet and Janin (1994).

In a terrain-following coordinate system, the wet/dry point treatment is no longer valid as D becomes zero. One simple way to avoid numerical singularity is to specify zero velocities at all dry points. This approach, however, cannot ensure volume conservation in the numerical computation due to discontinuous water removal from elements that turn to dry over one time step. An alternative way is to add a viscous boundary layer (D_{min}) at the bottom and redefine wet/dry points using a sum of D and D_{min}. The grid is treated as a wet point for $D > D_{min}$, otherwise it is a dry point. In terms of the nature of the vertical structure of turbulent mixing, a viscous layer always exists below the log boundary layer near a solid wall (Wilcox, 2000). However, to avoid adding additional water transport into a dynamic system, the viscous layer should be sufficiently small to satisfy a motionless condition. In most of FVCOM applications, we recommend a value of $D_{min} = 5$ cm (Chen et al., 2006a,b, 2013).

No matter which methods are used to simulate the flooding/draining process over the land and intertidal wetlands, they must be validated with respect to mass conservation. In all of these methods, the dry and wet points are determined using some empirical criteria, so that the estimation of the water transport in the dry-wet transition zone depends on (1) the criterion used to define the wet/dry points, (2) the time step used for numerical integration, (3) the horizontal and vertical resolutions of the model grids, (4) amplitudes of surface elevation, and (5) bathymetry. In a terrain-following coordinate transformation model, it might be also related to the thickness of the bottom viscous layer (D_{min}).

A new wet/dry point treatment method was developed for use with FVCOM (Chen et al., 2006b, 2008a,b). This method has been validated in a series of tidal simulations using an idealized semi-enclosed estuary with an inter-tidal zone. Relationships of the time step with discrete grid resolution, amplitude of external forcing, the slope of the intertidal zone and thickness of the bottom viscous layer are discussed and the criterion for the selection of the time step has been derived (Chen et al., 2006b, 2013). The rule used in validation is mass conservation, which, we believe, is a prerequisite condition for an objective evaluation of the wet/dry point treatment technique in estuaries (and coastal regions where inundation occurs). A detailed description of the criteria used to determine the wet and dry points can be found in the FVCOM User Manuals (Chen et al., 2004, 2006b and 2013) and a brief summary is given here.

Defining that $D = H_m + \zeta$, where $D = H_m + D_{min}$ in the water and $H_m = -(h_B + D_{min})$ on the land (Fig. A1), the wet or dry criterion for node points is given as

$$\begin{cases} \text{wet}, & \text{if } D = H_m + \zeta > D_{min} \\ \text{dry} & \text{if } D = H_m + \zeta \leqslant D_{min} \end{cases}$$

and for triangular cells is given as

$$\begin{cases} \text{wet}, & \text{if } D = \min(H_{m,i}, H_{m,\hat{j}}, H_{m,\hat{k}}) + \max(\zeta_{\hat{i}}, \zeta_{\hat{j}}, \zeta_{\hat{k}}) > D_{min} \\ \text{dry}, & \text{if } D = \min(H_{m,i}, H_{m,\hat{j}}, H_{m,\hat{k}}) + \max(\zeta_{\hat{i}}, \zeta_{\hat{j}}, \zeta_{\hat{k}}) \leqslant D_{min} \end{cases}$$

where D_{min} is the thickness of the viscous layer specified at the bottom, h_B is the bathymetric height related to the edge of the main channel of a river (Fig. A1) and $\hat{i}$, $\hat{j}$, and $\hat{k}$ are the integer numbers to identify the three node points of a triangular cell.

When a triangular cell is treated as dry, the velocity at the centroid of this triangle is specified to be zero and no flux is allowed on the three boundaries of this triangle. This triangular cell is removed from the flux calculation in the TCE. For example, the integral form of the continuity equation in FVCOM is written as

$$\int\int_{TCE} \frac{\partial \zeta}{\partial t} dxdy = -\int\int_{TCE} \left[\frac{\partial(\bar{u}D)}{\partial x} + \frac{\partial(\bar{v}D)}{\partial y} \right] dxdy = -\oint_l \bar{v}_N D dl \tag{A.3}$$

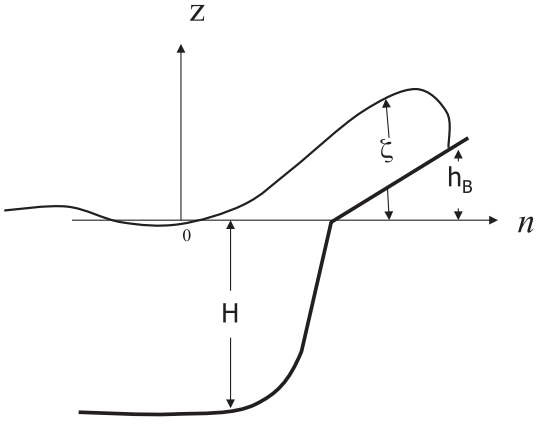

Fig. A1. Illustration of a cross-shelf section for an idealized coast with definition of H, ζ and h_B.

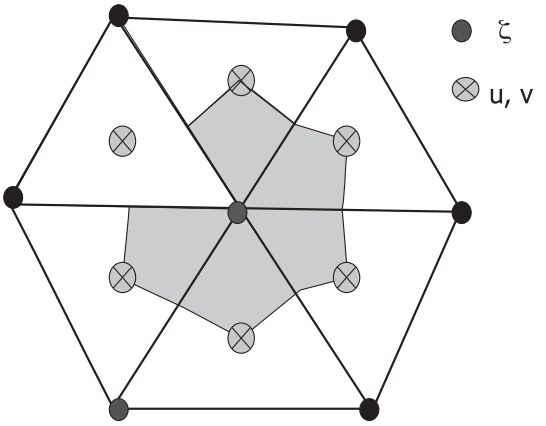

Fig. A2. Illustration of dry and wet segments of a tracer control element.

where $\bar{u}$ and $\bar{v}$ are the x and y components of the vertically-averaged velocity. In a dry/wet point system, only wet triangles are taken into account in the flux calculation in a TCE since the flux on boundaries of the dry triangle is zero (see Fig. A2). This approach always ensures the volume conservation in a TCE that contains the moving boundary between the dry and wet triangles over an integration interval. The same approach is used to calculate the tracer flux (temperature, salary and other scalar tracers) and momentum flux in a MCE.

One of the critical issues in applying the wet/dry point treatment technique in a split-mode model is to ensure mass conservation in the individual TCE which is crossed by the moving boundary. In a mode-split model, an adjustment must be made in every internal time step to ensure the consistency in the vertically integrated water transport produced by external and internal modes (Chen et al., 2004). In FVCOM, if the σ-coordinates are used, for example, the vertical velocity at the σ surface (ω) is calculated by

$$\omega_{i,k+1} = \omega_{i,k} + \frac{\Delta\sigma_k}{\Delta t_I}(\zeta_i^{n+1} - \zeta_i^n) + \frac{\Delta\sigma_k}{\Omega_i}\oint_l v_{N,k}^n Ddl, \tag{A.4}$$

where i, k, and n is indicators of the ith node point, kth σ level and nth time step, respectively; Ω_i^n is the area of the ith TCE at the nth time step. N is an indicator of the velocity component normal to the boundary of a TCE with a length of l. To conserve the volume on the ith TCE, the vertically integrated form of Eq. (A.4) must satisfy

$$\frac{\zeta_i^{n+1} - \zeta_i^n}{\Delta t_I} + \sum_{k=1}^{kb-1}\frac{\Delta\sigma_k}{\Omega_i^n}\oint_l v_{N,k}^n Ddl = 0 \tag{A.5}$$

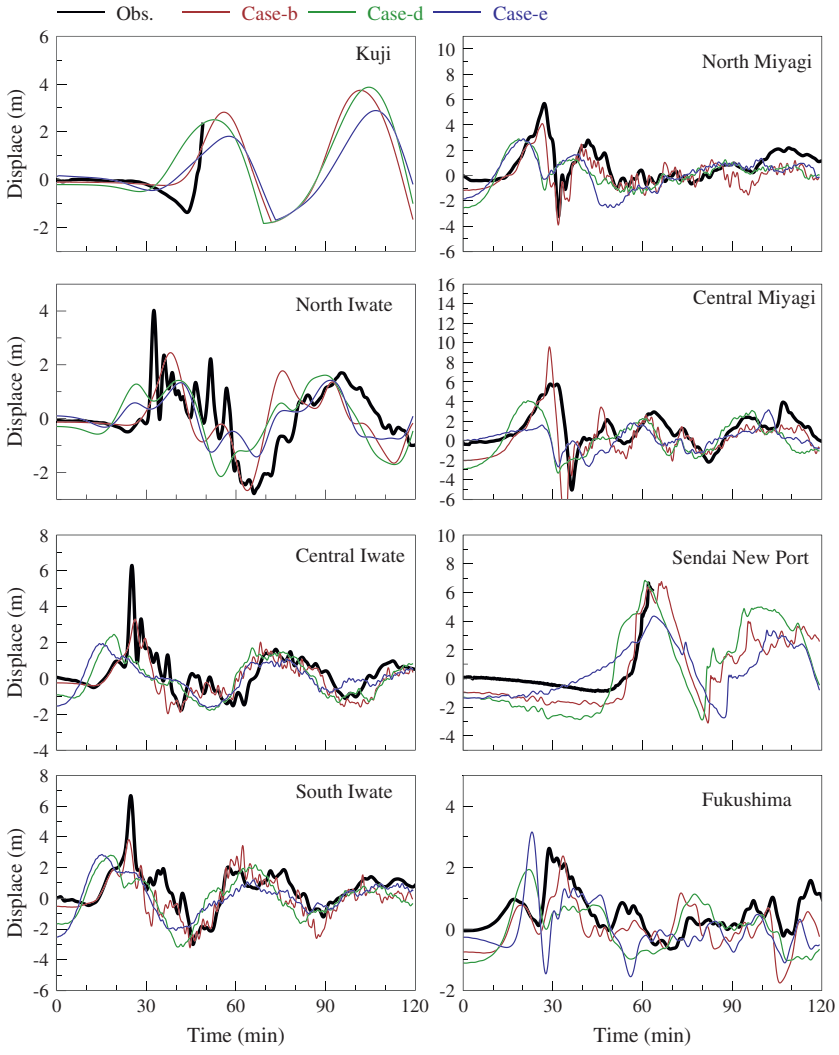

Fig. B1. Comparisons of the model-simulated and observed sea level displacement (m) at eight tide gauges (location shown in Fig. 1) over the initial 120-min period for the model runs with initial conditions of the seafloor change specified by case-b, case-d and case-e.

Please cite this article in press as: Chen, C., et al. The March 11, 2011 Tōhoku M9.0 earthquake-induced tsunami and coastal inundation along the Japanese coast: A model assessment. Prog. Oceanogr. (2014), http://dx.doi.org/10.1016/j.pocean.2014.01.002

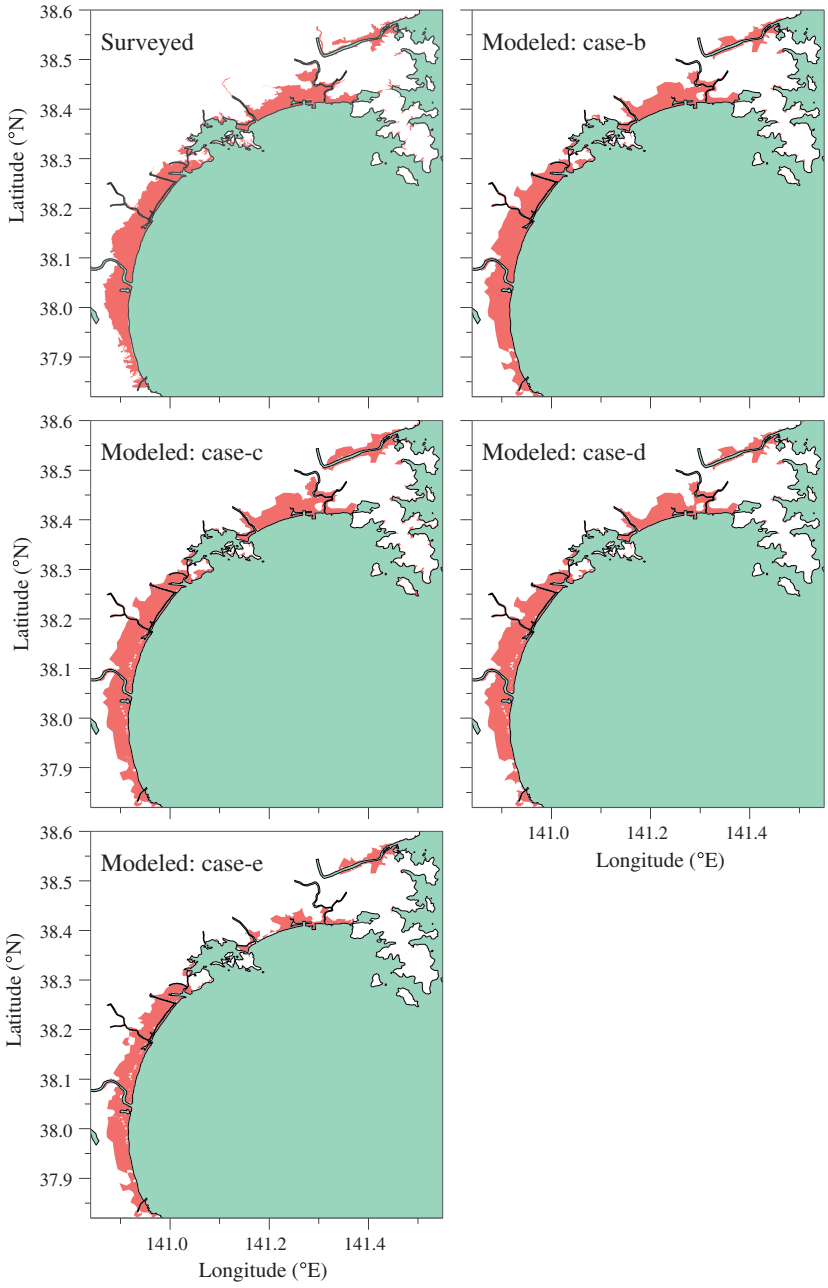

Fig. B2. Comparisons of model-predicted inundation areas with the surveyed areas along the Miyagi coast for the initial condition cases of seafloor change specified by cases b–e.

where *kb* is the total number of the σ levels. Since ζ_i^{n+1} is calculated through the vertically integrated continuity equation over I_{split} external mode time steps (where $I_{split} = \frac{\Delta t_I}{\Delta t_E}$), Eq. (A.5) is valid only if

$$\Delta t_I \sum_{k=1}^{kb-1} \frac{\Delta\sigma_k}{\Omega_i^n} \oint_l v_{N,k}^n Ddl = \Delta t_E \sum_{n=1}^{I_{split}} \frac{i}{\Omega_i^{\bar{n}}} \oint_l \bar{v}_N^{\bar{n}} Ddl. \tag{A.6}$$

Because the numerical accuracy depends on the time step, the left and right sides of Eq. (A.6) is not exactly equal to each other unless $I_{split} = 1$. Therefore, to ensure the conservation of the volume transport throughout the water column of the *i*th TCE, the internal velocity in each σ-layer must be calibrated using the difference of an inequality of vertically integrated external and internal water transport before ω is calculated. Since the vertically integrated transport features the barotropic motion, the easiest calibration way is to adjust the internal velocity by distributing the "error" uniformly throughout the water column. ω, which is calculated with adjusted internal velocities through Eq. (A.4), not only guarantees that the volume transport is conservative in the whole water column but also in an individual TCE volume in each σ layer. Because the water temperature and salinity or other tracers are calculated in the same TCE volume as that used for ω, this transport adjustment also conserves the mass in an individual TEC volume in each σ layer. When the wet/dry point treatment is calculated, however, because $\Omega_i^{\bar{n}}$ may change within I_{split} external time integrations due to the occurrence of dry triangles and ζ is treated as zero when D is less than D_{min}, we have:

$$\zeta_i^{n+1} - \zeta_i^n \neq \Delta t_E \sum_{n=1}^{I_{split}} \frac{1}{\Omega_i^{\bar{n}}} \oint_l \bar{v}_N^{\bar{n}} Ddl. \tag{A.7}$$

Please cite this article in press as: Chen, C., et al. The March 11, 2011 Tōhoku M9.0 earthquake-induced tsunami and coastal inundation along the Japanese coast: A model assessment. Prog. Oceanogr. (2014), http://dx.doi.org/10.1016/j.pocean.2014.01.002

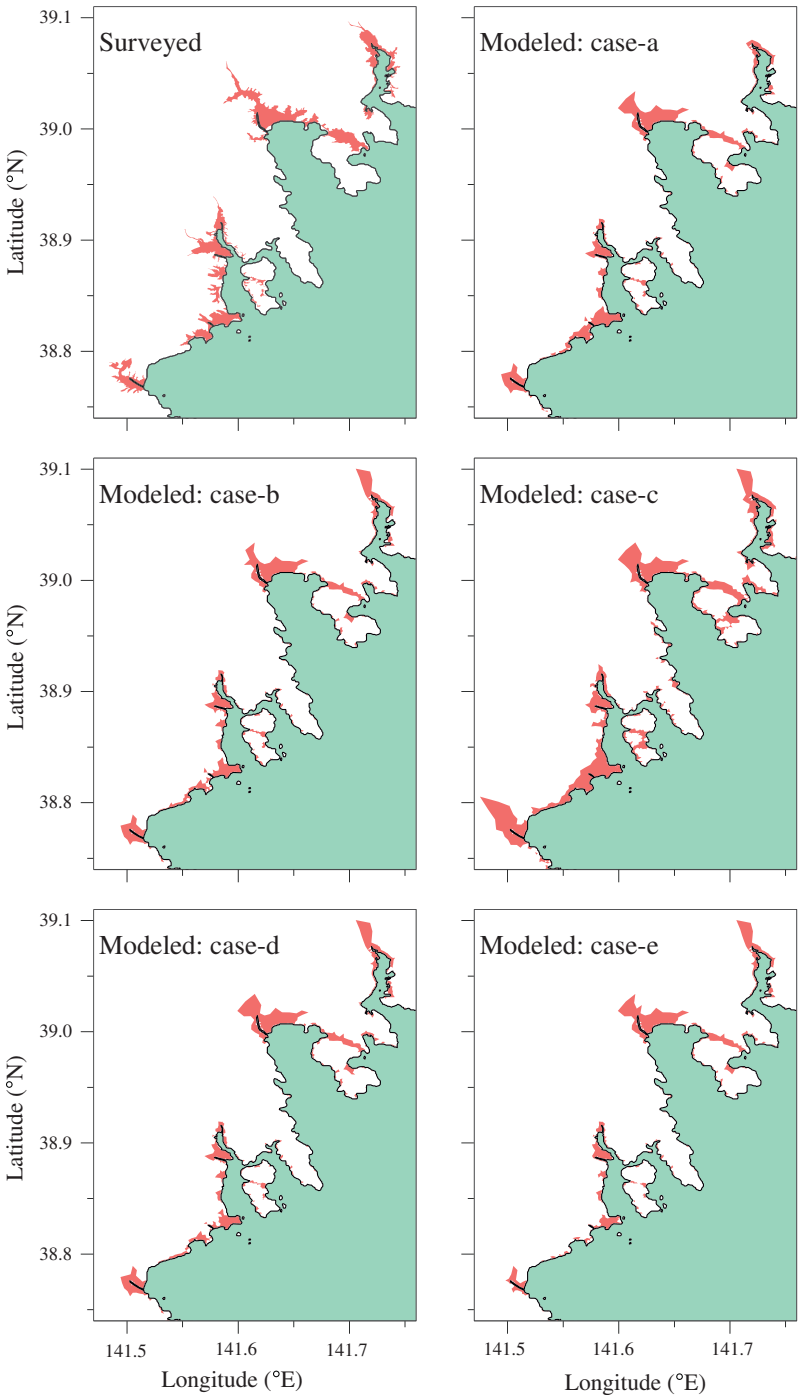

Fig. B3. Comparisons of model-predicted inundation areas with the surveyed areas in the southern region of the Iwate coast for the five initial condition cases of seafloor change specified by cases a–e.

In this case, the external and internal mode adjustment through Eq. (A.6) cannot guarantee that ω reaches zero at $\sigma = -1$ for the internal mode. To ensure the volume conservation, an additional adjustment for ζ_i^{n+1} must be made in the TCE when ω is calculated by Eq. (A.5). The additional sea level adjustment works in general, but fails in the case where ζ is very close to D_{min} (for example, $\Delta\zeta = \zeta - D_{min} < 10^{-1}$ cm). When this happens, small errors in the calculation of volume flux can rapidly accumulate through nonlinear feedback of tracer advection terms and eventually destroy the nature of the mass conservation. The additional sea level adjustment works in general, but fails in the case where ζ is very close to D_{min} (for example, $\Delta\zeta = \zeta - D_{min} < 10^{-1}$ cm). FVCOM always ensures the mass conservation in the wet–dry transition zone if $I_{split} = 1$. For computational efficiency, however, we want to find an approach so that mass conservation is still guaranteed for the case in which $I_{split} > 1$. In additional to the criterion of general numerical instability, in a case with inclusion of the flooding/drying process, the choice of I_{split} is restricted by many other factors including the surface elevation, bathymetry, and thickness of the bottom viscous layer and horizontal/vertical resolutions. A discussion on the relationship of I_{split} to these factors was given in detail in the FVCOM User Manual with the update in Chen et al. (2013).

Please cite this article in press as: Chen, C., et al. The March 11, 2011 Tōhoku M9.0 earthquake-induced tsunami and coastal inundation along the Japanese coast: A model assessment. Prog. Oceanogr. (2014), http://dx.doi.org/10.1016/j.pocean.2014.01.002

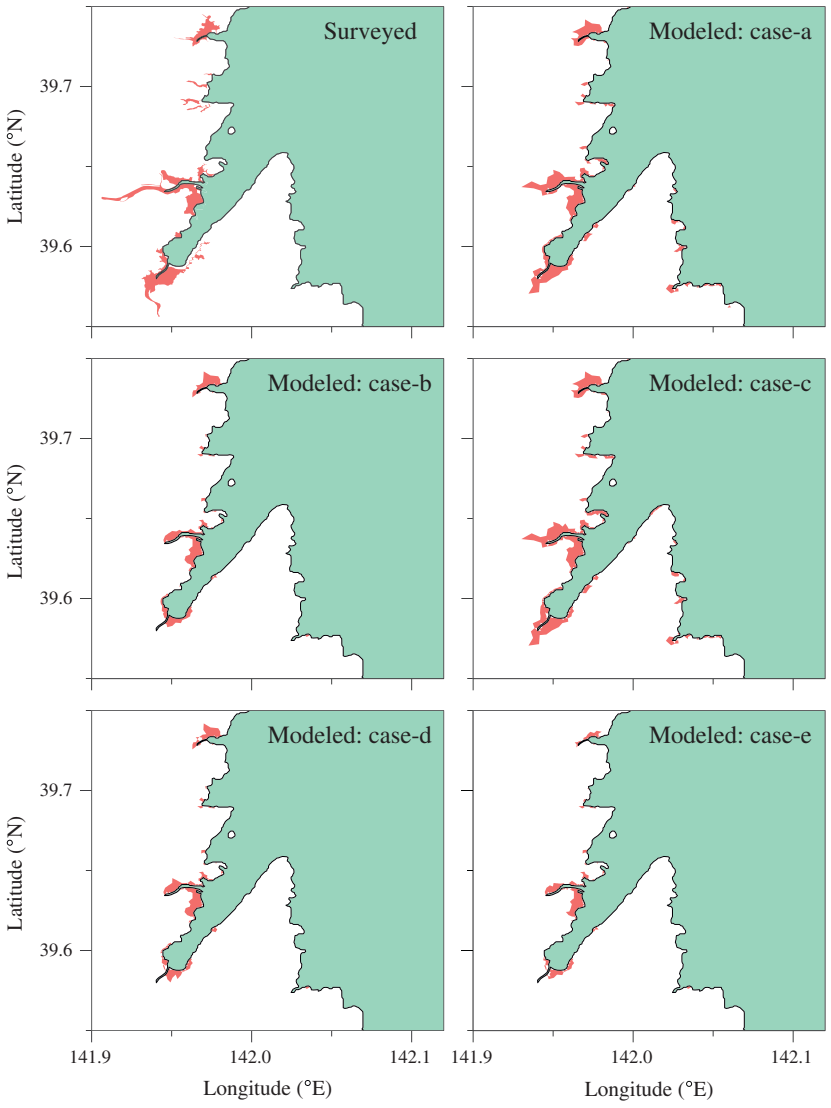

Fig. B4. Comparisons of model-predicted inundation areas with the surveyed areas in the northern region of the Iwate coast for the five initial condition cases of seafloor change specified by cases a–e.

The wet/dry point treatment method of FVCOM was validated by an application to simulate the tide-induced flooding/drying process in the estuarine-tidal creek-salt marsh complex of the Okatee/Colleton River Estuary, South Carolina (SC) (Chen et al., 2008b,c, and unpublished manuscripts). Hypsometric measurements were made using remote-sensing by Drs. Andrade and Blanton at Skidaway Institute of Oceanography the upstream area of the Okatee River during the flood period on November 9, 2001, during which the extent of the flooded area was accurately mapped with a time interval of about one hour. The model-data comparisons showed that FVCOM was capable of reproducing tidal and residual currents in the river and the time evolution of the flushing area onto salt marshes. This method succeeded in stimulating the flooding/draining process in the Satilla River estuary, Georgia (Chen et al., 2008c).

Appendix B. Model-data comparison for water elevations and inundation areas for five seismic model-predicted initial conditions

The model-predicted tsunami water levels for cases-b, d and e are shown and compared with observations at available tidal gauges in Fig. B1. Combined with cases-a and c shown in Fig. 9 in the text, it was clear that the model-predicted water level depended significantly on the initial condition of the sea level predicted by seismic models. The difference varied in space at different tidal gauges. At North Iwate, Central Iwate, and South Iwate in the northern area, case-c predicted the smallest water level differences with observations, but the timing was better in case-a at North Iwate and in case-b at Central Iwate and South Iwate. At Central Miyagi, case-a showed the best simulation for water level, and case-b predicted the best timing. At Sendai New Port, all five cases caught the first largest tsunami peak, not only in amplitude but also in timing. Case-b predicted the most accurate water level, and case-c showed the best timing. If one considered the overall performance based on both water level and phase, case-a was better at this site. At Fukushima, case-b and case-a were the best in amplitude and timing, respectively.

The model-predicted inundation areas made for the five seismic initial conditions are shown and compared with observations in Fig. B2 (region-I), Fig. B3 (region-II) and Fig. B4 (FDNPP). Although the model-predicted inundation areas for these five cases were in reasonable agreement with observations, it was clear that a significant error occurred in the more rugged area north of Central

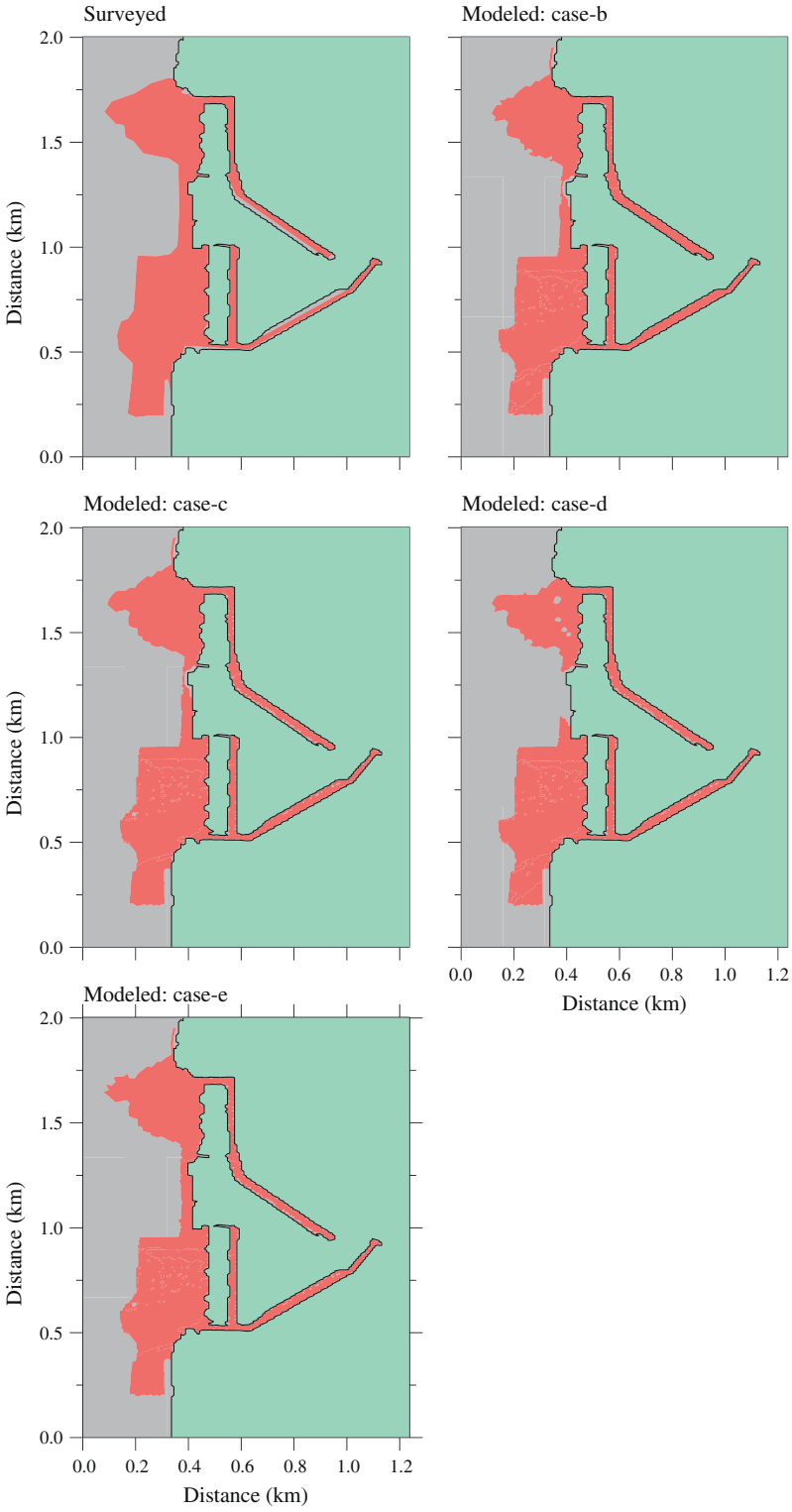

Fig. B5. Comparisons of model-predicted inundation areas with the surveyed area in the Fukushima Dai-ichi Nuclear Power Plant region for the initial condition cases of seafloor change specified by cases b–e.

Miyagi, which included several rivers. In this region, cases a–d all were capable of reproducing the inundated spots, but the model-predicted areas at these sports differed from measurements, particularly in the inland areas of the rivers. This was partially due to the relatively lower accuracy of the coastal zone bathymetry and land elevation in these areas and decreased grid resolution along this northern shore. The model results for all five cases were described in detail in the text based on Table 2. Fig. B4 provides a view of the model-predicted flooded areas in and around FDNPP for cases b–e (see Fig. B5).

References

Austria, P.M., Aldama, A.A., 1990. Adaptive mesh scheme for free surface flows with moving boundaries. In: Gambolati, G., Rinaldo, A., Brebbiam, C.A., Fray, W.G., Pinder, G.F. (Eds.), Computational methods in Surface Hydrology. Springer-Verlag, New York, pp. 456–460.

Beardsley, R.C., Chen, C., Lai, Z., Sasaki, J., Lin, H., Lin, J., Ji, R., 2012. A US–Japan collaborative research on assessment of the March 11 2011 Earthquake, Tsunami Inundation and Initial Spread of Fukushima Dai-ichi Radionuclides into the Pacific Ocean. The 2012 Ocean Science Meeting, Salt Lake City. Abstract and Poster.

Carrier, G., Greenspan, H.P., 1958. Water waves of finite amplitude on a sloping beach. J. Fluid Mech. 4, 97–109.

Casulli, V., Cheng, R.T., 1991. A semi-implicit finite-difference model for three-dimensional tidal circulation. In: Spaulding, M. et al. (Eds.), Proceeding of 2nd International Conference on Estuarine and Coastal Modeling. ASCE, Tampa, Florida, pp. 620–631.

Casulli, V., Cheng, R.T., 1992. Semi-implicit finite-difference methods for three-dimensional shallow-water flow. Int. J. Numer. Meth. Fluids 15, 629–648.

Casulli, V., Cattani, E., 1994. Stability, accuracy and efficiency of a semi-implicit method for three-dimensional shallow water flow. Comput. Math. Appl. 27, 99–112.

Chan, I.C., Liu, P.L.F., 2012. On the runup of long waves on a plane beach. J. Geophys. Res. 117, C08006. http://dx.doi.org/10.1029/2012JC007994.

Chen, C., Liu, H., Beardsley, R.C., 2003. An unstructured grid, finite-volume, three dimensional, primitive equations ocean model: application to coastal ocean and estuaries. J. Atmos. Ocean Technol. 20 (1), 159–186.

Chen, C, Cowles, G., Beardsley, R.C., 2004. An Unstructured Grid, Finite-volume Coastal Ocean Model: FVCOM User Manual, Second Edition. SMAST/UMASSD Technical Report-04-0601, p. 183.

Chen, C., Beardsley, R.C., Cowles, G., 2006a. An unstructured grid, finite-volume coastal ocean model (FVCOM) system. Special Issue entitled "Advances in Computational Oceanography". Oceanography 19 (1), 78–89.

Chen, C., Cowles, G., Beardsley, R.C., 2006b. An Unstructured Grid, Finite-volume Coastal Ocean Model: FVCOM User Manual, Second Edition, SMAST/UMASSD Technical Report-06-0602, p. 315.

Chen, C., Huang, H., Beardsley, R.C., Liu, H., Xu, Q., Cowles, G., 2007. A finite-volume numerical approach for coastal ocean circulation studies: comparisons with finite difference models. J. Geophys. Res. 112, C03018. http://dx.doi.org/10.1029/2006JC003485.

Chen, C., Qi, J., Li, C., Beardsley, R.C., Lin, H., Walker, R., Gates, K., 2008a. Complexity of the flooding/drying process in an estuarine tidal-creek salt-marsh system: an application of FVCOM. J. Geophys. Res. 113, C07052. http://dx.doi.org/10.1029/2007jc004328.

Chen, C., Qi, J., Liu, H., Beardsley, R.C., Lin, H., Cowles, G., 2008b. A Wet/Dry Point Treatment Method of FVCOM, Part-I: Stability Experiments. Unpublished manuscript.

Chen, C., Huang, H., Lin, H., Blanton, J., Li, C., Andrade, F., 2008c. A Wet/Dry Point Treatment Method of FVCOM, Part II: Application to the Okatee/Colleton River in South Carolina. Unpublished manuscript.

Chen, C., Beardsley, R.C., Cowles, G., Qi, J., Lai, Z., Gao, G., Stuebe, D., Liu, H., Xu, Q., Xue, P., Ge, J., Ji, R., Hu, S., Tian, R., Huang, H., Wu, L., Lin, H., Sun, Y., Zhao, L., 2013. An Unstructured-grid, Finite-volume Community Ocean Model FVCOM User Manual, third ed. SMAST/UMASSD Technical Report-13-0701, University of Massachusetts-Dartmouth, p. 404.

Davies, A.M., Jones, J.E., Xing, J., 1997. Review of recent developments in tidal hydrodynamic modeling, I: Spectral models. J. Hydraulic Eng. ASCE 123, 278–292.

EERI, 2012. The 2010 Canterbury and 2011 Christchurch New Zealand Earthquakes and the 2011 Tohoku Japan Earthquake: Emerging Research Needs and Opportunities. Workshop Report <http://www.eeri.org/japan-new-zealand-nsf-rapid-workshop/>.

Flather, R. A., N. S. Heaps, N. S., 1975. Tidal computations for Morecambe Bay. Geophys. J. Roy. Astr. Soc., 42:489-517.

Fritz, H.M., Phillips, D.A., Okayasu, A., Shimozono, H., Liu, H., Mohammed, F., Skanavis, V., Synolakis, C.E., Takahashi, T., 2012. The 2011 Japan tsunami current velocity measurements from survivor videos at Kesennuma Bay using LiDAR. Geophys. Res. Lett. 39, L00G23. http://dx.doi.org/10.1029/2011GL050686.

Fujii, Y., Satake, K., Sakai, S., Shinohara, M., Kanazawa, T., 2011. Tsunami source of the 2011 off the Pacific coast of Tohoku earthquake. Earth Planets Space 63, 815–820. http://dx.doi.org/10.5047/eps.2011.06.010.

Hayes, G.P., 2011. Rapid source characterization of the 2011 Mw 9.0 off the Pacific coast of Tohoku Earthquake. Earth Planets Space 63 (7), 529–534. http://dx.doi.org/10.5047/eps.2011.05.012.

Hervouet, J.M., Janin, J.M., 1994. Finite-element algorithms for modeling flood propagation. In: Molinaro, P., Natale, L. (Eds.), Modeling of Flood Propagation Over Initially Dry Areas. ASCE, New York, pp. 102–113.

Hu, S., Chen, C., Gao, G., Lai, Z., Ge, J., Lin, H., Qi, J., 2012. Preliminary analysis on the simulation of the East China Sea of the Global-FVCOM model. J. Shanghai Ocean Univ. 21 (4), 621–629.

Ip, J.T.C., Lynch, D.R., Friedrichs, C.T., 1998. Simulation of estuarine flooding and dewatering with application to Great Bay, New Hampshire. Estuar. Coast. Shelf Sci. 47, 119–141.

Keller, J.B., Keller, H.B., 1964. Water Wave Run-up on a Beach, PNR Research Rep. NR-3828(00), Dep. of the Navy, Washington, DC.

Kim, K.O., Choi, B.H., Min, B., 2011. Three Dimensional Simulation of 2011 East Japan-off Pacific Coastal Earthquake Tsunami Induced Vorticity in the Oarai Port. The Pacific Ocean Tsunami (in Korean Language), Korean Society of Coastal and Ocean Engineers, Printed by Hanrimwon Co., Ltd., pp. 58–65.

Lai, Z., Chen, C., Beardsley, R.C., Lin, H., Ji, R., Sasaki, J., Lin, J., 2013. Initial spread of ^{137}Cs from the Fukushima Dai-ichi Nuclear Power Plant over the Japan continental shelf: a study using a high-resolution, global-coastal nested ocean model. Biogeosciences 10, 5439–5449. http://dx.doi.org/10.5194/bg-10-5439-2013.

Leendertse, J.J., 1970. A Water-quality Simulation Model for Well-Mixed Estuaries and Coastal Seas: Principles of Computation, Rand Corporation, Report RM-6230-RC, vol. I.

Leendertse, J.J. 1987. Aspects of SIMSYS2D, A System for Two-Dimensional Flow Computation. Rand Corporation, Report R-3572-USGS.

Lynch, D.R., Gray, W.G., 1980. Finite element simulation of flow in deforming regions. J. Comput. Phys. 36, 135–153.

Lynett, P., Borrero, J.C., Weiss, R., Son, S., Greer, D., Renteria, W., 2012. Observations and modeling tsunami-induced currents in ports and harbors. Earth Planet. Sci. Lett. 327–328, 68–74.

Madsen, P.A., Schäffer, H.A., 2010. Analytical solutions for tsunami runup on a plane beach: single waves, N-waves and transient waves. J. Fluid Mech. 645, 27–57.

Mori, N., Takahashi, T., Yasuda, T., Yanagisawa, H., 2011. Survey of 2011 Tohoku earthquake tsunami inundation and run-up. Geophys. Res. Lett. 38, L00G14. http://dx.doi.org/10.1029/2011GL049210.

Pollitz, F., Bürgmann, R., Banerjee, P., 2011. Geodetic slip model of the 2011 M9.0 Tohoku earthquake. Geophys. Res. Lett. 38, L00G08. http://dx.doi.org/10.1029/2011GL048632.

Sasaki, J., Ito, K., Kazunori, I., Suzuki, T., Wiyono, R.U.A., Oda, Y., Takayama, Y., Yokota, K., Furata, A., Takagi, H., 2012. Behavior of the 2011 Tohoku earthquake tsunami and resultant damage in Tokyo Bay. Coast. Eng. J. 54 (1). http://dx.doi.org/10.1142/So57856341250012 (1250012 (1–16)).

Sasaki, J., Komatsu, T., Matsumaru, R., Wiyono, R.U.A., 2011. Unstructured model investigation of 2004 Indian Ocean tsunami inundation in Banda Aceh, Indonesia. J. Coast. Res. SI64, 941–945 (ICE2011 (Proceedings), ISSN0749-0208).

Shao, G., Li, X., Ji, C., Maeda, T., 2011. Focal mechanism and slip history of the 2011 M_w 9.1 off the Pacific coast of Tohoku earthquake, constrained with teleseismic body and surface waves. Earth Planets Space 63, 559–564. http://dx.doi.org/10.5047/eps.2011.06.028.

Sidén, G.L.D., Lynch, D.R., 1988. Wave equation hydrodynamics on deforming elements. Int. J. Numer. Meth. Fluids 8, 1071–1093.

Simons, M., Minson, S.E., Sladen, A., Ortega, F., Jiang, J., Owen, S.E., Meng, L., Ampuero, J.-P., Wei, S., Chu, R., Helmberger, D.V., Kanamori, H., Hetland, E., Moore, A.W., Webb, F.H., 2011. The 2011 magnitude 9.0 Tohoku-Oki earthquake: Mosaicking the megathrust from seconds to centuries. Science 332, 1421–1425. http://dx.doi.org/10.1126/science.1206731.

Stein, S., Wysession, M., 2003. An Introduction to Seismology, Earthquakes, and Earth Structure. Blackwell Publishing, Oxford, UK, 498 pp (ISBN 0865420785).

Synolakis, C.E., 1987. The runup of solitary waves. J. Fluid Mech. 185, 523–545.

Synolakis, C.E., Bernard, E.N., Titov, V.V., Kânoglu, U., González, F., 2008. Validation and verification of tsunami numerical models. Pure Appl. Geophys. 165, 2197–2228.

Toda, S., Lin, J., Stein, R.S., 2011. Using the 2011 Mw 9.0 off the Pacific coast of Tohoku Earthquake to test the Coulomb stress triggering hypothesis and to calculate faults brought closer to failure. Earth Planets Space 63, 725–730.

USGS, 2011. Earthquake Information Bulletin: Magnitude 9.0, Near the East Coast of Honshu, Japan. U.S. Geological Survey, National Earthquake Information Center. <http://earthquake.usgs.gov/earthquakes/recenteqsww/Quakes/usc0001xgp.php>.

Wei, S., Sladen, A., 2011. Tohoku Source Model v.1. <http://www.tectonics.caltech.edu/slip history/2011_taiheiyo-oki/>.

Wilcox, D.C., 2000. Turbulence Modeling for CFD. DCW Industries, Inc., 540pp.

Yagi, Y., Fukahata, Y., 2011. Rupture process of the 2011 Tohoku-Oki earthquake and absolute elastic strain release. Geophys. Res. Lett. 38, L19307. http://dx.doi.org/10.1029/2011GL048701.

Yoon, B.S., Bae, J.S., Lim, C.H., 2011. Propagation characteristics of the Pacific coast of Tohoku tsunami in South Sea of Korea. The Pacific Ocean Tsunami (in Korean Language), Korean Society of Coastal and Ocean Engineers, Printed by Hanrimwon Co., Ltd., pp. 48–52.

Zheng, L., Chen, C., Liu, H., 2003. A modeling study of the Satilla River Estuary, Georgia. Part I: Flooding/drying process and water exchange over the salt marsh-estuary-shelf complex. Estuaries 26 (3), 651–669.

Please cite this article in press as: Chen, C., et al. The March 11, 2011 Tōhoku M9.0 earthquake-induced tsunami and coastal inundation along the Japanese coast: A model assessment. Prog. Oceanogr. (2014), http://dx.doi.org/10.1016/j.pocean.2014.01.002